2017

Application of an Optimized Expert System in Development of Simplified Turbomachinery Modelling

Matheson West
University of Windsor

Application of an Optimized Expert System in Development of Simplified Turbomachinery Modelling

by

Matheson West

A Thesis
Submitted to the Faculty of Graduate Studies
through the Department of Mechanical, Automotive & Materials Engineering
in Partial Fulfillment of the Requirements for
the Degree of Master of Applied Science at the
University of Windsor

Windsor, Ontario, Canada

2017

Application of an Optimized Expert System in Development of Simplified Turbomachinery Modelling

by

Matheson West

APPROVED BY:

N. Biswas
Department of Civil & Environmental Engineering

B. Minaker
Department of Mechanical, Automotive & Materials Engineering

J. Defoe, Advisor
Department of Mechanical, Automotive & Materials Engineering

September 28, 2017

Declaration of Originality

I hereby certify that I am the sole author of this thesis and that no part of this thesis has been published or submitted for publication.

I certify that, to the best of my knowledge, my thesis does not infringe upon anyone's copyright nor violate any proprietary rights and that any ideas, techniques, quotations, or any other material from the work of other people included in my thesis, published or otherwise, are fully acknowledged in accordance with the standard referencing practices. Furthermore, to the extent that I have included copyrighted material that surpasses the bounds of fair dealing within the meaning of the Canada Copyright Act, I certify that I have obtained a written permission from the copyright owner(s) to include such material(s) in my thesis and have included copies of such copyright clearances to my appendix.

I declare that this is a true copy of my thesis, including any final revisions, as approved by my thesis committee and the Graduate Studies office, and that this thesis has not been submitted for a higher degree to any other University or Institution.

Abstract

Simulating the ingestion of non-uniform inflow to a fan or compressor requires enormous computational resources if the full details of the flow in the blade rows being studied is to be resolved, since full-wheel unsteady computations are required. A simplified modelling approach exists as an alternative computational option, which is the use of volumetric source terms (body forces) in place of the physical blades. Typically, body force models are manually calibrated with reference to single passage simulation results, and demands significant user experience and expertise. The objective of this thesis is to eliminate the need for experience and expertise during model calibration as much as is practical by employing an automated expert system. The modelling approach employed in this work is the combination of an existing turning force model, and an adaptation of an existing viscous force model. The automated system is implemented into Matlab and makes use of Ansys CFX as the flow solver. User input is required to initialize the system but the procedure then runs through to convergence of the final, calibrated model. Viscous force model coefficients that are traditionally found through an iterative procedure, are instead subjected to a Nelder-Mead optimization process. The machine studied as an example of the application of the automated technique is the NASA stage 67 transonic compressor. At peak efficiency, the isentropic rotor and stage efficiency, and the rotor work coefficient are matched within 1% of their single passage counterparts, a result that is on par with a manually generated body force model. A key finding in this thesis is that the stage efficiency is not the optimal parameter used for calibration of the stator's viscous force model. Despite this finding, the model produced performs sufficiently at off-design conditions not nearing choke. Across the speedline simulated, the model predicts the rotor total temperature ratio, total pressure ratio, and the stage total pressure ratio to within 1.3% of the single passage result. The computational time required for the calibration of the model produced from this work is 23 core-days. Although this computational cost remains relatively high, the removal of nearly all required user experience is achieved.

Acknowledgements

The work presented in this thesis is the result of the combined effort and support of the people I am fortunate enough to have close to me. Most importantly, I am thankful for the guidance and support of my advisor, Dr. Jeff Defoe. I owe a great deal of the knowledge and skills I employ today to him, as he has patiently guided me over the last few years. The dedication and focus he invests into each of his students is a testament to the type of professional he is, something I am truly grateful for. Also, I would like to thank my committee members Dr. Nihar Biswas and Dr. Bruce Minaker for their time in reviewing my thesis and insightful suggestions on improvements.

To the members of the Computational Fluid Dynamics Laboratory and Turbomachinery and Unsteady Flows groups who I was fortunate enough to cross paths with during my tenure, I would like to thank you for the advice and support you provided me that aided me in completing this thesis. Specifically, I would like to acknowledge David Jarrod Hill, Kharuna Ramrukheea, Quentin Minaker, and Kohei Fukuda.

As well, I would like to acknowledge the financial support I was granted from the Natural Sciences and Engineering Research Council.

Finally, I would like to thank my family: my parents, David and Jacqui and my brother JD. Without their endless support and unwavering belief, I would not be where I am today.

Contents

List of Figures

List of Tables

Nomenclature

Symbols

AR aspect ratio

B number of blades

c blade chord

e specific total energy

f volumetric source term per unit mass

F volumetric source term per unit volume

$\mathcal{F}$ objective function

FPR fan/compressor pressure ratio

h enthalpy, staggered spacing in blade row

K_n Peters volumetric source term coefficient

$\dot{m}$ mass flow rate

M Mach number

$\hat{n}_\theta$ circumferential projection of the local blade unit normal vector

p pressure

$\dot{Q}$ rate of heat transfer

r radial coordinate

s blade pitch

U blade speed

V absolute velocity

W relative velocity

$\dot{W}$ energy source per unit volume

x, y, z Cartesian coordinates

α absolute swirl angle

β relative swirl angle

δ flow deviation angle

ϵ compressibility correction factor

η efficiency

θ circumferential coordinate

κ local blade camber angle

Λ re-cambering constant

ρ density

σ blade solidity

υ relative grid density

ϕ axial flow coefficient

ψ rotor work coefficient

Ω fan rotational speed

Subscripts

BF body force

in inlet

is isentropic

LE leading edge

max maximum

min minimum

n direction normal to streamline

out outlet

p direction perpendicular to streamline

ref reference

rel relative

SP single passage

t total/stagnation quantity

TE trailing edge

Superscripts

M mass-averaged quantity

Abbreviations

CCL CFX Command Language

CFD Computational Fluid Dynamics

RANS Reynolds-Averaged Navier-Stokes

RMS Root Mean Squared

URANS Unsteady Reynolds-Averaged Navier-Stokes

Chapter 1

Introduction

Numerically simulating circumferentially and radially non-uniform flow through a fan or compressor is computationally expensive since obtaining the full details of the flow within the blade rows normally requires full-wheel, unsteady (time-accurate) computations. It is important to assess these flow fields due to the effects non-uniform flow can have on efficiency and unsteady rotor blade loading. Simulating a variety of inlet distortions becomes problematic with the computational cost limiting the ability to obtain results in a timely fashion. An existing approach to simplify the simulations replaces the physical blades with volumetric source term models (body force models) such as those used in Refs. [1, 2, 3]. Body force models typically consist of a force field normal to the local flow direction responsible for modelling the flow turning, as well as a force field locally parallel to the local flow direction that is responsible for modelling the viscous losses through the blade row. The model replaces the physical blades with a domain consistent with the blade row swept volume, and the force fields are added to the momentum equations within that volume; this is illustrated in Figure 1-1. As well, for rotors, the tangential force and rotational speed appear in the energy equation to give rise to stagnation enthalpy changes. Typically, when developing body force models, significant time and expertise is required as model calibration involves "tuning" of (iterating upon the values of) model coefficients to maximize the level of agreement with results produced by higher-fidelity, single-passage computations with uniform inflow. The motivation for this thesis is to provide an alternative option for

non-experts by producing an automated model development system.

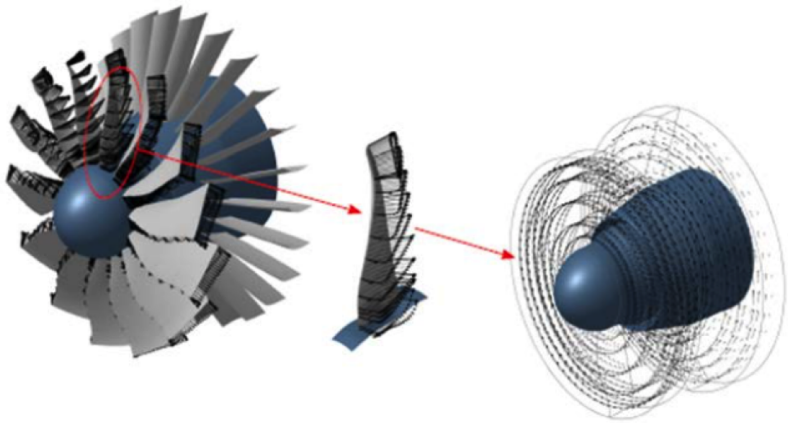

Figure 1-1: Body force field in the swept volume of the actual blade row [4]. Used with permission.

1.1 Objective and High-Level Approach

The objective of this thesis is to automate, as much as is practical, the process of body force model calibration. The automated model's accuracy is intended to be consistent with that of a user-generated version of the model. The modelling approach applied is largely based on Hill's work [1]; the contribution of this thesis is the automation of the model calibration process. The approach consists of a turning force and a viscous loss force for each blade row. A stage consisting of a rotor followed by a stator is assumed. Turning force model calibration involves using blade geometry data plus single passage computation results including flow angles and swirl (tangential) velocity. Traditional viscous force model calibration involves matching isentropic efficiency across a range of flow coefficients by manually tuning model coefficients. A second objective is applying an optimization process to determine the values of the viscous modelling coefficients, with the objective function being the root mean squared (RMS) error between isentropic efficiency reported from high-fidelity simulations and the model's reported value across a range of flow coefficients.

1.2 Challenges

Normally the body force model calibration process involves the use of several software packages and users manually move data between these tools. Therefore, automated data interchange and minimizing the movement of data between software packages are important challenges to address. Another obstacle faced when developing the automated system is determining when the model is sufficiently accurate. This involves specifying convergence criteria for each of the iteratively-determined aspects of the modelling approach. Setting the values for the convergence criteria is done with reference to previously conducted work on the same turbomachine used for development in this thesis [1]. The final challenge faced during system development is the generalization of the approach to account for any blade row. This challenge involves converting hard-coded parameters for the machine used during this study to functions capable of accepting user input for the machine of interest.

1.3 Major Findings and Conclusions

The system developed eliminates the majority of previously required user interaction during model calibration, as outlined in Ref. [1]. User input is required to initialize the automation scheme but the procedure then runs automatically through to convergence of the final model coefficient values. The system successfully produces a turning and viscous force model for the machine of interest with general agreement with the single passage results within 1% across the relevant parameters at the peak efficiency operating condition, as seen in Chapter 4. The computational cost of the model calibration process is approximately 23 core-days on modern systems; however, once the model is calibrated the computational cost of a full-wheel non-uniform inflow computation is at least two orders of magnitude smaller than that of a full-wheel unsteady Reynolds-averaged Navier-Stokes (URANS) solution. The advantage of the modelling approach becomes apparent when examining a variety of non-uniform flow conditions. The system is designed to produce a model for both a rotor and stator

blade row. Following the user input, the system is sufficiently robust to extract all relevant data provided by the user and incorporate it into the models of both the viscous and turning forces.

1.4 Thesis Outline

Relevant past literature is reviewed in Chapter 2, relating to body force modelling, expert systems, and optimization procedures. Next, the approach employed for the automated system is discussed in depth in Chapter 3. The assessment of the model's results and the final version of the model for a sample compressor is discussed in Chapter 4. Lastly, conclusions and potential improvements to the system for future work are detailed in Chapter 5.

Chapter 2

Literature Review

This chapter details the state of the art with regard to existing expert systems, optimization processes where an analytical version of the objective function is unknown, and body force modelling methodology. The expected contribution of the thesis is also outlined.

2.1 Body force modelling

Body force modelling was introduced by Marble[2] as replacing the physical blade row by an infinite number of infinitely-thin blades. The body forces are then broken down into a normal force per unit mass, f_n, and parallel force per unit mass, f_p. The normal force acts perpendicular to the relative streamlines, working to reduce the deviation of the flow from the blade camber surface (the locus of blade camber lines from hub to tip). The parallel force acts against the streamwise direction and generates viscous losses in the flow. These two forces are illustrated in Figure 2-1.

While studying short-wavelength stall inception and distortion transfer in multistage compressors, body force modelling was expanded upon by Gong[3]. Unlike Marble's implementation, Gong's model distributes source terms axially and radially which allows the model to respond to local flow properties. Viscous effects are only captured in the body force implementation in this approach; the flow outside the blade rows is assumed inviscid. The Euler equations including the body force

implementation are:

$$\frac{\partial}{\partial t}\begin{bmatrix} r\rho \\ r\rho V_x \\ r\rho V_r \\ r\rho V_\theta \\ r_\rho e_t \end{bmatrix} = \frac{\partial}{\partial x}\begin{bmatrix} r\rho V_x \\ r\rho V_x^2 + r\rho \\ r\rho V_x V_r \\ r\rho V_x V_\theta \\ rV_x(\rho e_t + p) \end{bmatrix} + \frac{\partial}{\partial r}\begin{bmatrix} r\rho V_r \\ r\rho V_r V_x \\ r\rho V_r^2 + rp \\ r\rho V_r V_\theta \\ rV_r(\rho e_t + p) \end{bmatrix}$$
$$+ \frac{\partial}{\partial \theta}\begin{bmatrix} \rho V_\theta \\ \rho V_\theta V_x \\ \rho V_\theta V_r \\ \rho V_\theta^2 + p \\ V_\theta(\rho e_t + p) \end{bmatrix} = \begin{bmatrix} 0 \\ rF_x \\ \rho V_\theta^2 + p + rF_r \\ -\rho V_r V_\theta + rF_\theta \\ r\left(\vec{F}\cdot\vec{V} + \dot{Q}\right) \end{bmatrix}, \tag{2.1}$$

where the force per unit volume, $\overrightarrow{F}$, and force per unit mass, $\vec{f}$, are related through the local density,

$$\overrightarrow{F} = \begin{bmatrix} F_x \\ F_\theta \\ F_r \end{bmatrix} = \rho\vec{f} = \rho \begin{bmatrix} f_x \\ f_\theta \\ f_r \end{bmatrix} \tag{2.2}$$

and the volumetric energy source term is

$$\dot{W} = \rho\overrightarrow{f}\cdot\overrightarrow{V} + \dot{Q} \tag{2.3}$$

If the flow is considered to be adiabatic ($\dot{Q} = 0$),

$$\dot{W} == \rho f_\theta \Omega r, \tag{2.4}$$

where ρ is the local density, r is the radial coordinate, $\vec{V}$ is the absolute velocity, p is the static pressure, Ω is the rotational speed, e is the specific total energy, and $\dot{Q}$ is the rate of heat transfer; the rate of work added to the flow at each spatial location is a product of the circumferential component of the body force term, ρf_θ, and the

circumferential blade velocity, Ωr. At each spatial location within a blade row, the rate of total enthalpy rise per unit volume is given by Equation 2.4. If the reader desires a detailed description of the development of the current state of the art in body force modelling, Hill's recent thesis provides an excellent overview as of early 2017 [1]. In particular, see Section 2.4 of Hill's thesis. In the remainder of this section only work directly applicable to the current thesis is discussed.

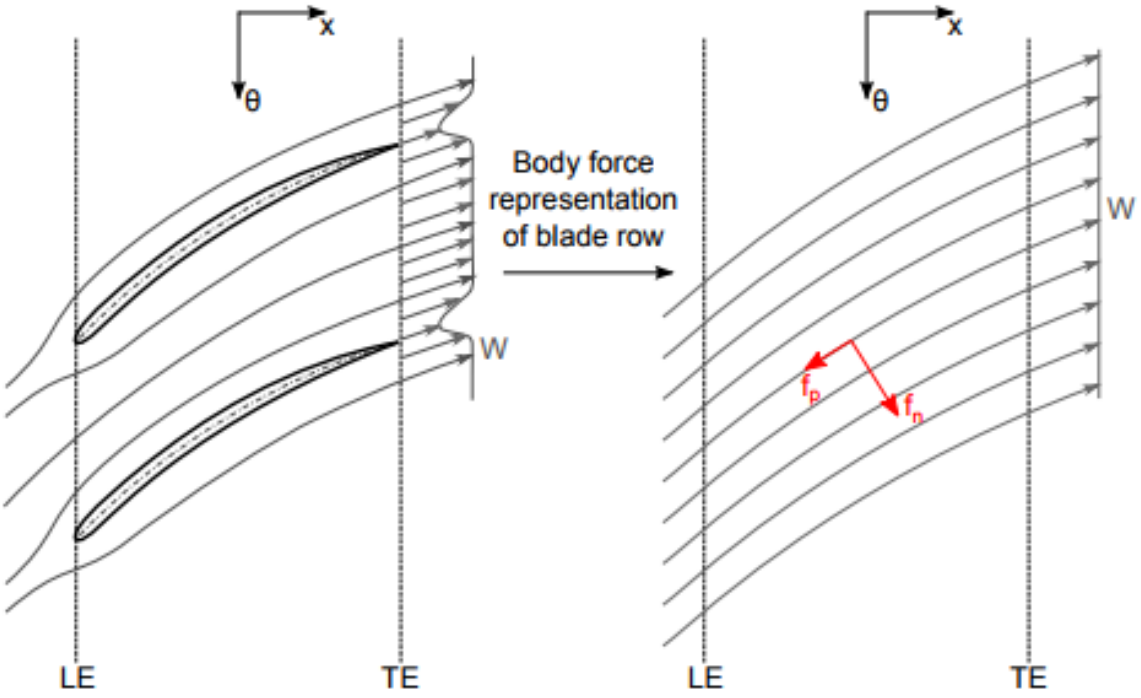

Figure 2-1: Body force terms: normal turning force and parallel viscous force [4]. Used with permission.

Peters' model adapted Gong's model to investigate fan inlet and nacelle design parameters for low pressure ratio fans [4]. Peters' modification to Gong's model includes a radial component in the normal force, which accounted for blade lean and radial streamline shifts due to area contractions. Peters' expansion of Gong's parallel force model included an off-design formulation with the purpose of capturing the variation in blade losses with operating condition. Peters' formulation uses a mix of quadratic dependence on mass-averaged relative Mach number at the blade row inlet, as well as the existing quadratic dependence on local relative velocity:

$$f_p = \frac{K_{p1}}{h}\left[(\overline{M}_{rel}^{M})^2 + K_{p2}(\overline{M}_{rel}^{M} - M_{ref})^2\right]W^2, \tag{2.5}$$

where K_{p1} and K_{p2} are viscous force coefficients, $\overline{M}_{rel}^{M}$ is the mass averaged relative Mach number at the blade row inlet, and M_{ref} is the value of $\overline{M}_{rel}^{M}$ at peak efficiency, W is the local relative velocity, and h is the staggered blade spacing,

$$h = \frac{2\pi r\sqrt{\sigma}cos\kappa}{B}. \tag{2.6}$$

Here κ is the local blade camber angle, B is the number of blades, and σ is the blade solidity,

$$\sigma = \frac{c}{s}, \tag{2.7}$$

where c is the blade chord length and s is the blade pitch. This formulation produces the desired quadratic loss profile associated with turbomachines. A diagram depicting h, κ, c, and s can be found in Figure 2-2. Peters' model is calibrated for a specific rotational speed, which produces a speedline for varying flow coefficient. The term 'speedline' refers to a performance assessment across a range of operating conditions, using performance metrics such as the isentropic efficiency, total pressure ratio, or total temperature ratio. Varying the rotational speed would require updated model calibration constants.

In this thesis Peters' normal force model was not used as there is a discontinuity in Peters' model where the local deviation angle is zero. In order to account for this, an offset constant was implemented in [4]; this is extensively covered in Section 2.4.2 of Hill[1]. Hill showed that this model poorly predicts the desired slope of the efficiency vs. flow coefficient curve due to the use of the offset constant. The use of the offset constant is unavoidable due to zero-value local flow deviations across the blade, which is why Hall's[5] normal force model is instead chosen for use in this thesis. Hall's approach is outlined in detail next.

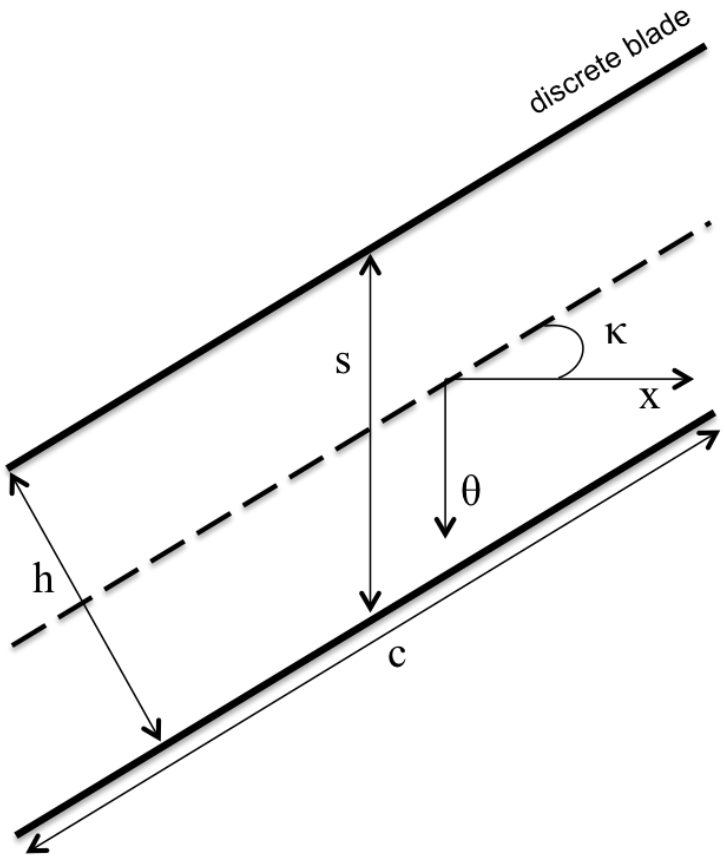

Figure 2-2: Simplified diagram depicting blade geometry parameters.

An incompressible, inviscid body force model was developed by Hall et al.[5]. The inviscid assumption eliminates the need for a viscous model. The normal force model is a function of local flow quantities and blade camber angle, allowing the model to be formulated without the need of a single passage RANS calculation for calibration. The normal force per unit mass is expressed as

$$f_n = \frac{(2\pi\delta)\left(\frac{1}{2}W^2/\left|\hat{n}_\theta\right|\right)}{2\pi r/B}, \tag{2.8}$$

where $\hat{n}_\theta$ is the circumferential projection of the local blade unit normal vector and δ is the local deviation angle. However, this approach is limited by the fact that there is no mechanism to model the effects of blade metal blockage and that it only yields accurate models in low-speed flows, due to its assumption of incompressible flow.

To capture flow compressibility and blade metal blockage effects, two modifications

developed at the University of Windsor by Hill[1] are added to Hall's normal force modelling approach. An addition to the deviation term (ϵ) captures compressibility effects by matching the relative flow angles produced by the body force model with those reported from circumferential averages of single passage simulations:

$$\begin{aligned} f_n &= \frac{2\pi\left(\delta+\epsilon\right)\frac{1}{2}W^2}{2\pi r\left|\hat{n}_\theta\right|/B} \\ f_n &= \frac{\left(\delta+\epsilon\right)W^2}{2r\cos\kappa/B}. \end{aligned} \tag{2.9}$$

where the substitution $|\hat{n}_\theta| = \cos\kappa$ has been made; this trigonometric relationship can be visualized in Figure 2-3.

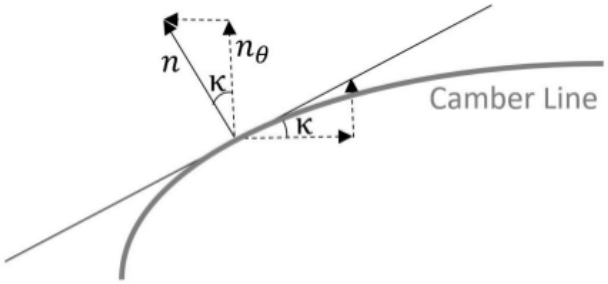

Figure 2-3: Example blade camber line used to illustrate the relationship between $\cos\kappa$ and $|\hat{n}_\theta|$.

The compressibility correction is an iteratively determined spatially-varying function that alters the local blade angle for the rotor and stator so that the local normal force is adjusted appropriately. Hall's normal force model, Equation 2.8, is simulated at peak efficiency for the rotational speed of interest, and the relative flow angles are extracted from the results within the rotor domain in the $x-r$ plane. These relative flow angles are subtracted from the circumferentially-averaged, peak efficiency, single-passage flow angles, as illustrated in Figure 2-4. This ensures that leading edge incidence is well-captured in the body force model, the relative flow angles are enforced within the rotor, and the absolute flow angles are enforced within the stator.

The second modification applies only to rotating blade rows to ensure that the

correct work is done on the flow by the rotor. The importance of this modification can be seen from the Euler turbine equation,

$$h_{t,out} - h_{t,in} = \Omega(r_{out}V_{\theta,out} - r_{in}V_{\theta,in}), \tag{2.10}$$

where h_t is the total enthalpy, V_θ is the absolute-frame swirl velocity, and r is the radial coordinate. For the body force model to produce the same total enthalpy rise as the single-passage computations, the Euler turbine equation makes it clear that the absolute swirl velocities at rotor outlet must match assuming the upstream flows are the same. This correction is necessary due to the fact that blade metal blockage is not directly modelled in the body force approach. The blade camber surface model is altered so that at the trailing edge, the correct tangential velocity is obtained. The re-camber is linearly increased from zero at the leading edge to the full amount required at the trailing edge; the implementation details are discussed in Section 3.4.6. These two changes together ensure that both leading edge incidence and trailing edge work input are correctly captured by the normal force model.

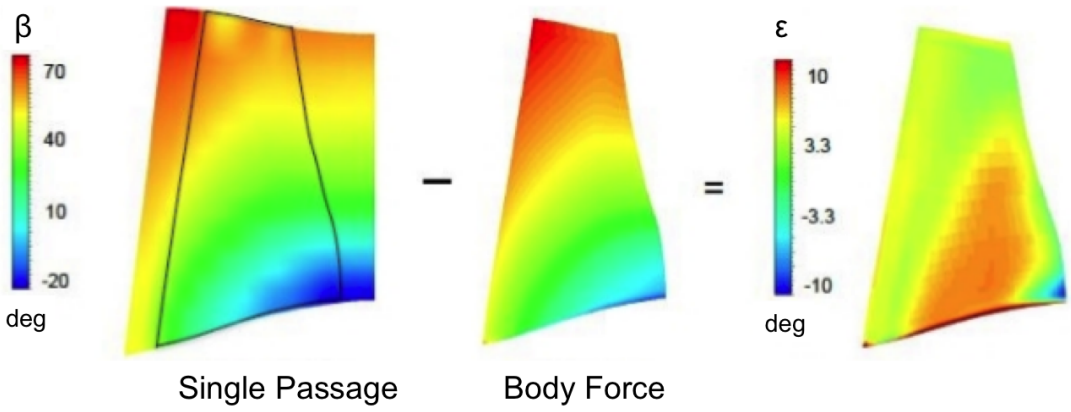

Figure 2-4: One iteration of the ϵ extraction process [1]. Used with permission.

Hill's work also produced an updated version of Peters' loss model. To increase the model's robustness in predicting efficiency vs. flow coefficient curves, two innovations were implemented. The reference Mach number is no longer necessarily located at the peak efficiency point, and separate coefficients are implemented above and below

the peak efficiency Mach number. This allows for enhanced control of the efficiency characteristic shape, as the quadratic slope on either side of peak efficiency is not necessarily the same. The force formulation thus becomes

$$f_{p,new} = \begin{cases} f_p & if\ \overline{M}_{rel}^{M} < M'_{ref} \\ f_p \left[1 + K'_{p2} \left(M'_{ref} - \overline{M}_{rel}^{M} \right)^2 \right] & if\ \overline{M}_{rel}^{M} > M'_{ref} \end{cases}, \tag{2.11}$$

where f_p is Peters' loss model detailed in equation 2.5, K'_{p2} is a constant used to alter the efficiency at flow coefficients where $\overline{M}_{rel}^{M} > M'_{ref}$. In this thesis, a simplified version of the double-sided model is used as the parallel force model, and is outlined in Section 3.4.7.

2.2 Expert Systems

An expert system is a computer program that uses artificial intelligence methods to solve problems within a specialized domain that ordinarily requires human expertise [6]. Typically, an expert system relies on two components: a knowledge base and an inference engine. The inference engine interprets and evaluates the data in the knowledge base to provide an "answer" [6]. For example, research conducted by Seok et al.[7] produced an expert system capable of determining bone age based on expert data. The expert data for this work came from interviewing a pediatric endocrinologist and a radiologist. The "knowledge base" in this instance is the expert data collected from the interviews, and the "inference engine" is the algorithm itself. The algorithm produces the overall bone age of a hand following an input of X-ray images of the left hand. Another example of an expert system comes from work conducted by Ikram et al.[8]. The system produced by this work is capable of predicting earthquakes using a knowledge base of earthquake data from 1972 to 2013. The algorithm requires an input of the longitude, latitude, magnitude, and depth of a current earthquake, and predicts the location and magnitude of a resultant earthquake. Based on this existing research, it can be deemed that traditional elements of an expert system are an

inference engine and knowledge base. Although the system presented in this thesis does not fall within the traditional definition of an expert system, it has expert system qualities, involving the application of expert knowledge (a previously-developed body force modelling approach and resultant model [1]) to obtain a body force model without the need for user interaction during model development. The knowledge base can be thought of as the level of agreement between the model and the single passage calculations, the form of the model functions, and the default number of points on the speedline used for optimization; the inference engine can be thought of as the algorithm itself.

Previously conducted research in the areas of computational fluid dynamics (CFD) and automated modelling do not incorporate automated model development, but instead incorporate automated model selection for the user-supplied problem description. For example, Koziel et al.[9] produced a system that selects grid and flow parameters which are typically chosen by a user while optimizing airfoil shape. Depending on the resultant parameters, the system then chooses the "best-choice" CFD model for the shape of the airfoil. The main advantage of Koziel's system is the reduction in computational time when compared to conventional low-fidelity model development. The automated turbomachinery model development system presented in this thesis is therefore something that has not been done before.

2.3 Optimization

Numerical optimization typically involves three fundamental elements: an objective function to be minimized or maximized, a collection of variables whose values are manipulated to optimize the objective, and a set of constraints to restrict the values that the variables can take. Typical optimization employs the objective function's derivatives to determine the maximum or minimum [10]. Optimizing an objective function whose analytical form is unknown is typically done through the use of gradient-free optimization methods. The most commonly used gradient-free methods are the Nelder-Mead simplex, genetic algorithms, and particle swarm optimization. While

all of these methods provide suitable approaches when optimizing objective functions with unknown gradients, they are typically used for problems with large numbers of variables; however, the Nelder-Mead method performs best with few design variables. The genetic algorithm and particle swarm optimization procedures are considered "brute force" methods that require a large number of function evaluations [11]. As outlined in Section 3.4.7, the number of variables being optimized in this thesis is two. This suggests the Nelder-Mead method is the best optimization method for this problem.

The Nelder-Mead method was developed by J. A. Nelder and R. Mead. The method minimizes a function of n variables, which depends on the comparison of function values at the $n+1$ vertices of a general simplex, followed by the replacement of the vertex with the highest value by a new vertex. A simplex is a structure in n-dimensional space formed by $n+1$ points that are not in the same plane. For example, a line segment is a 1-dimensional simplex, a triangle is a 2-dimensional simplex and a tetrahedron is a simplex in 3-dimensional space [11]. The simplex adapts itself to the local landscape, and contracts on the final minimum [12]. Research conducted by Osgood et al.[13] employed the Nelder-Mead method as their objective function could not be expressed analytically. Osgood's work involved an objective function of the sum of squared errors between image coordinates from a camera and re-projected laser data. Another example of the use of the Nelder-Mead method can be found in work conducted by Abedi et al.[14]. That research involved optimizing a metal-organic chemical vapour deposition process. The objective function's gradients were unknown, leading to the use of the Nelder-Mead method. The objective function was the deviation in thickness of deposited gas film since the aim was to achieve uniform thickness of the film. One of the known disadvantages of the Nelder-Mead method is the relatively slow convergence when dealing with large number of variables. Since the proposed optimization scheme in this work is constrained to two variables, and an analytical version of the objective function is unknown, the Nelder-Mead method is deemed suitable and is selected for use in the optimization procedure.

2.4 State of the Art and Limitations of Previous Research

When developing a body force model, the current state of the art requires a user to manually develop the model. This involves "tuning" the model constants, as well as post-processing the model results; to conduct these steps effectively, significant user expertise is required. Eliminating the need for user expertise can be achieved through the use of an automated system. The viscous model development that is typically conducted by "tuning" the model coefficients could instead by subjected to an optimization process, specifically the Nelder-Mead method. To the author's knowledge, no work has been conducted to produce an automated expert system with these capabilities.

To achieve this improvement to the state of the art, the model development process is implemented in Matlab [15], while making use of Ansys CFX [16] for the CFD computations. Automated data input is conducted via CFX-Pre session files, while data output is conducted via CFD-Post session files. The implementation of the automated system is explained in detail in Chapter 3.

Chapter 3

Approach

Typically, the models described in Section 2.1 require significant user experience to calibrate, and the processing of data produced by the model and the higher-fidelity single passage computations required for calibration is also a task which typically requires significant user experience and effort. This chapter describes the functionality and use of an automated system that eliminates the majority of user expertise and interaction required to obtain a well-calibrated model. The automated system requires user input to commence model development. The input required is as follows:

- single passage geometry and the grid for the blade row(s) of interest;
- the corrected rotational speed of the machine, or the speed of the machine if the inlet temperature corresponded with ambient conditions at sea level;
- the peak-efficiency corrected mass flow rate of the machine at the given corrected speed;
- the operating points chosen for the speedline of interest; and
- the tolerance for convergence of the objective function and the variables being optimized related to the viscous force coefficients.

Step-by-step instructions on the model grid generation process is provided in Section 3.3 as automating this step is too complex at present. The complexity associated with

automating this step includes learning the scripting language Glyph, the language employed by the meshing software used in this work, Pointwise [17]. As well, implementing a portion of the automated system capable of understanding the underlying geometry associated with the machine being tested presents numerous challenges, and is beyond the scope of this work. This could serve as a future improvement of the system, as this would be a feature more typical of conventional "expert systems," as discussed in Section 2.2. The viscous model coefficients, typically found through an iterative procedure by the user, are instead optimized during automated model development. The objective function for this optimization process is the RMS error between single-passage computed isentropic efficiency and the model's reported isentropic efficiency across the speedline chosen by the user. The automated system is implemented in Matlab [15], which operates as a front-end with the Ansys tools CFX-Pre, CFX, and CFD-Post working in the background. The system executes CFX operations via Matlab's "system" function, and "cfx5pre", "cfx5solve", and "cfd-post" commands. Writing data into CFX case definition (.def) files, and exporting data from results (.res) files is achieved through the use of session files, which are essentially Perl scripts. Perl is a general-purpose, dynamic programming language that is used within CFX as the CFX Command Language (CCL). A high level overview of the model development process is depicted in Figure 3-1.

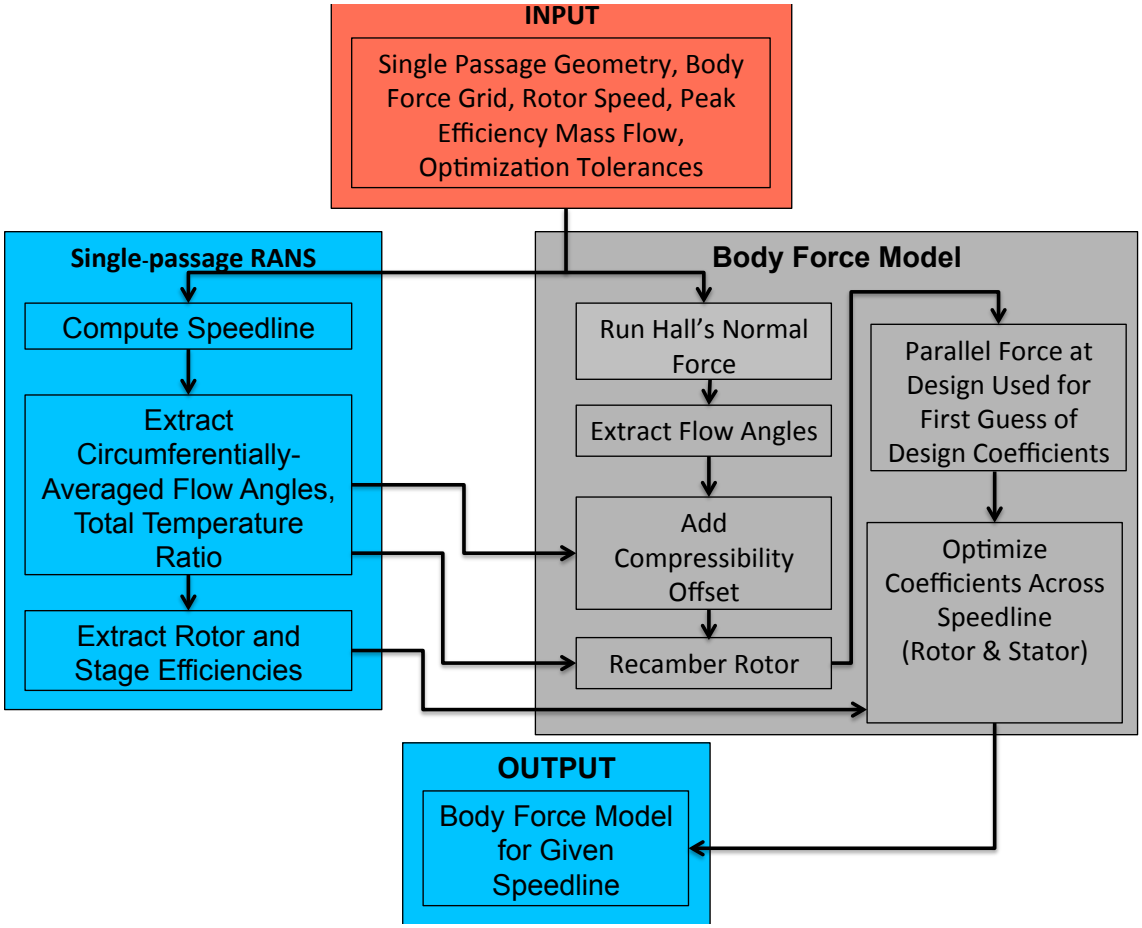

Figure 3-1: Process conducted during automated body force model development.

3.1 Machine Used for Assessment

In this work, the transonic compressor NASA stage 67 is used as a sample machine for assessment of the automation procedure. Important features for this machine are given in Table 3.1. This single-stage axial compressor is selected as it has both blade geometry and experimental results available in the open literature. As previously mentioned, research completed by Hill at the University of Windsor [1] provided a user-generated version of the model being produced in this thesis by the automated system. This serves as a baseline against which to compare the model generated by the automated approach. At 90% rotor speed, the tip relative Mach number is 1.20 [18] so that the compressibility corrections Hill developed are important. With an average hub-to-tip radius ratio of 0.427, the machine lies in between a fan and a

typical compressor. This means that the flow response is similar to that of a first stage compressor or a low bypass ratio fan in a turbofan engine.

Table 3.1: Important design characteristics for NASA Rotor 67 at 90% speed [18, 19].

Ω (rad/s)	1512	σ_{hub}	3.11
$M_{rel,tip}$	1.20	σ_{tip}	1.29
FPR	1.48	$\left(\frac{r_{hub}}{r_{tip}}\right)_{inlet}$	0.375
$\dot{m}$ (kg/s)	31.10	$\left(\frac{r_{hub}}{r_{tip}}\right)_{outlet}$	0.478
B	22	$\eta_{is}(\%)$	92.2
AR	1.56	$\phi = \frac{\overline{V_x}^M}{U_{mid}}$	0.50
$\frac{\text{tip clearance}}{r_{tip}}$ (%)	0.39		

In the table, FPR is the fan pressure ratio, σ is the blade solidity, η_{is} is the rotor isentropic efficiency, $\dot{m}$ is the mass flow rate, AR is the rotor blade aspect ratio, and ϕ is the flow coefficient. The rotor consists of 22 blades which rotate clockwise (facing downstream); the stator has 36 blades. A technical report produced by NASA has made blade data available for rotor 67 at 14 spanwise locations for the rotor [18], and 16 spanwise locations for the stator. At each of these locations, blade geometry is given in cylindrical coordinates, from blade leading edge to trailing edge, and back to the leading edge. Geometry for the upstream and downstream ducts are not available. Hill produced an artificial nose and inlet duct [1], in an attempt to match those used in Fidalgo et al.'s study [19], and this is the geometry used in this thesis. The nose is stationary; only a portion of the hub rotates with the rotor, as outlined in Figure 3-2. In this sense, the machine behaves as a compressor rather than a fan, as a fan would typically have a rotating nose.

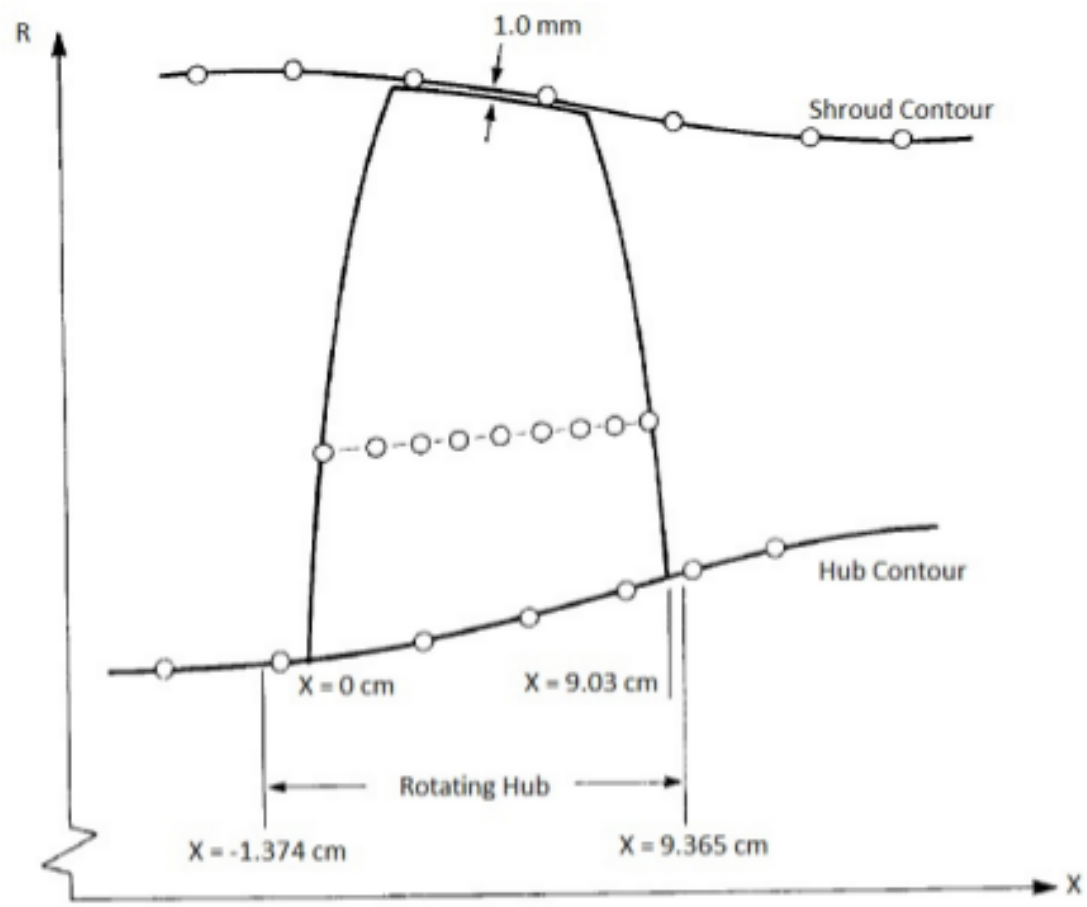

Figure 3-2: Rotational and non-rotational sections of the NASA Rotor 67 hub [18].

3.2 Single Passage Computations

As indicated in Figure 3-1, the single passage geometry is required for model development. This section serves to outline the steps taken in this study to obtain the single passage geometry and computational grid. Best practices for the single passage simulation set up can be found in Section 3.3 of Hill's thesis [1], and should be followed; for NASA stage 67, the single passage grid consists of 3.6 million cells. The single passage grid represents one blade passage, meaning 1/22 of the inlet and rotor region, and 1/36 of the stator and outlet regions for this stage. The single passage rotor and stator grid topologies are shown in Figure 3-3. This grid was generated by Hill [1], and made available for the sake of this research. The domain inlet por-

tion of the grid was created using Pointwise [17], while the remaining sections of the grid were created using ANSYS TurboGrid [20]. Due to the complexity of the grid near the physical blade, TurboGrid is the preferred software as it uses an automated grid generation algorithm, catered towards the study of turbomachinery. The NASA stage 67 rotor has a large stagger angle near the blade tip, and due to this stagger, the complexity of the grid is significantly increased in the outer span regions. For this reason, TurboGrid is especially useful in comparison to manual grid generation. A further advantage of TurboGrid is its handling of a non-conformal tip gap, as the rotor region requires a tip gap of $0.0039R_{tip}$ to allow rotor clearance while operating [1]. For a more detailed description of the single passage grid generation, please see Section 3.3.2 of Hill's thesis. Table 3.2 outlines grid count statistics, where the relative grid density, υ, is calculated as

$$\upsilon = \frac{\text{Cell}\,\%}{\text{Volume}\,\%}. \tag{3.1}$$

The Spalart-Almaras turbulence model is used with $y^+ < 30$. The boundary conditions are stagnation pressure and temperature at inlet and mass flow rate specified at outlet. Mixing planes are incorporated upstream and downstream of the rotor, or alternatively only between the rotor and stator. The convergence criterion is a conservation target for mass, momentum, and energy flux of $< 0.5\%$ and RMS residuals $< 1.0 \times 10^{-3}$. An illustration of the single passage computational domain used for this thesis can be found in Figure 3-4.

Table 3.2: Grid count statistics for both single passage and full annulus RANS calculations[1].

Region	Cell/Passage	Passage/360°	Cells/360°	Volume %	Cell %	v
Inlet	458,346	22	10,083,612	52.9	10.5	0.198
Rotor Inlet	106,848	22	2,350,656	8.42	2.44	0.290
Rotor	1,781,061	22	39,183,342	6.04	40.8	6.75
Stator	1,065,792	36	38,368,512	4.29	39.9	9.30
Outlet	171,600	36	6,177,600	28.4	6.42	0.226
Total	3,583,647		96,163,722			

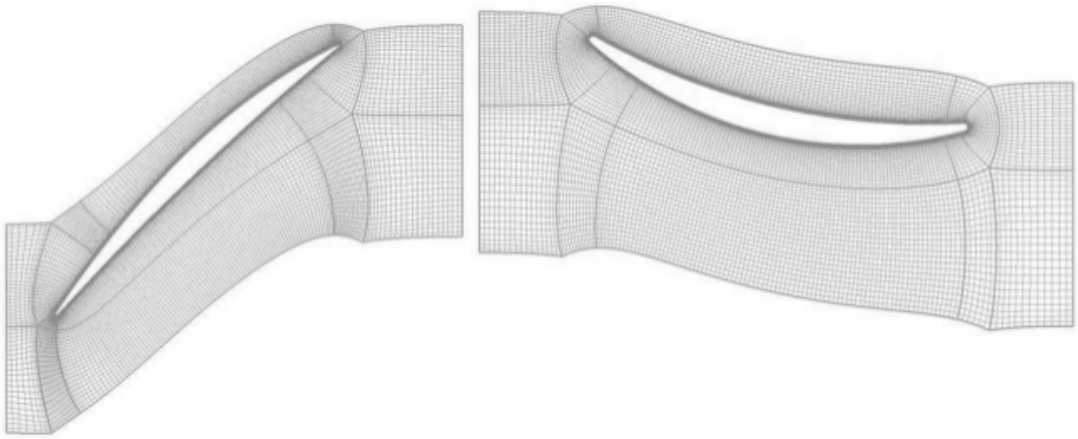

Figure 3-3: Single Passage rotor (left) and stator (right) grid topologies at midspan [1]. Flow is from left to right.

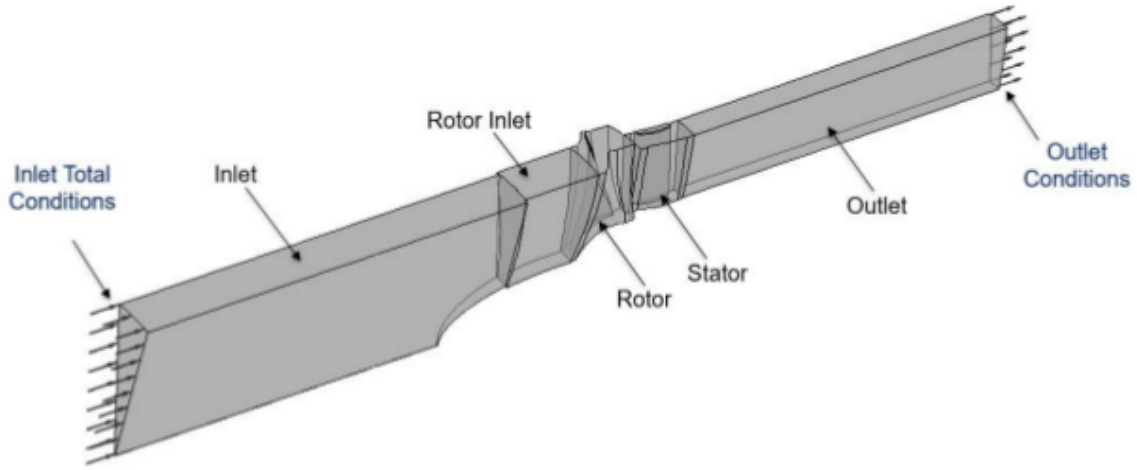

Figure 3-4: Single-passage domain as defined in CFX-Pre [1].

3.3 Body Force Grid Generation

The next required input for the automated system is the grid used for the body force computations, as indicated in Figure 3-1. The body force grid used during this work consists of a 3 degree slice of the full annulus. To decrease the required computational time for model development, the smallest possible computational domain was desired while still maintaining accurate computational capabilities. This grid corresponding with a 3 degree section of the full annulus was the smallest domain found to produce accurate results, as CFX does not have a 2D solver. The hub and casing curves as well as the leading and trailing edge projections onto the axial-radial plane for each blade row are required to generate the grid. Each blade row must be its own fluid "zone" (rotor and stator) as source terms are implemented into CFX by their respective "zone." The baseline grid use in this study contains 3 circumferential cells, 60 radial cells including hub and casing boundary layers, and 292 axial cells. The computational domain extends from 3 rotor diameters upstream of the rotor leading edge to 2 rotor diameters downstream of the stator trailing edge for this single-stage configuration. The axial cell division is as follows: 90 upstream of the rotor, 50 for the rotor, 30 for the rotor-stator gap, 50 for the stator, and 72 downstream of the stator. Figure 3-5 depicts a meridional projection of the grid; similar grid resolution

is recommended.

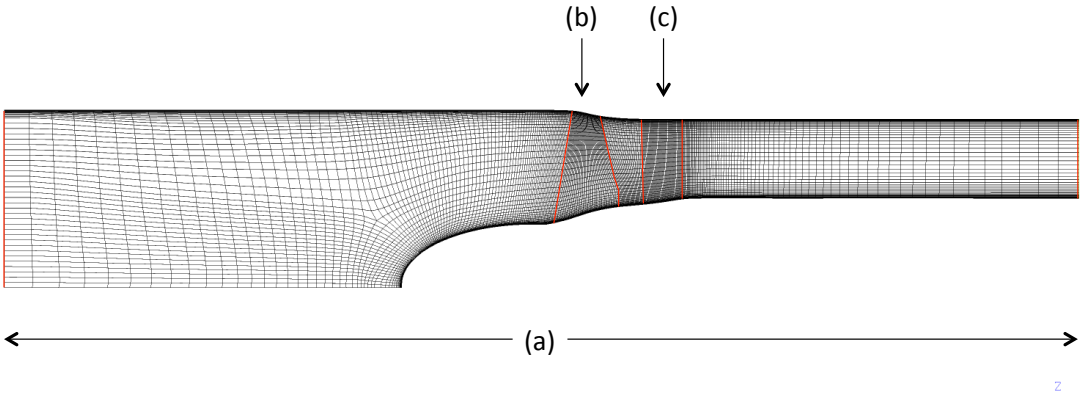

Figure 3-5: Meridional view of body force grid. (a) Complete computational domain; (b) rotor swept volume; (c) stator swept volume.

Grid independence is confirmed at 90% corrected speed; Table 3.3 quantifies the changes between a baseline and fine grid. The parameters used to monitor grid independence are the isentropic rotor efficiency, and the rotor work coefficient

$$\psi = \frac{\Delta h_t}{U^2}, \tag{3.2}$$

where Δh_t is the rise in total enthalpy across the rotor and U is the blade tip speed. The changes in both parameters are small enough that the baseline grid is sufficiently fine.

Table 3.3: Body force grid independence study.

	Baseline grid	Fine grid	% Change
Cell count	5.25×10^4	1.45×10^5	176%
Rotor work coefficient	0.2248	0.2263	0.67%
Rotor isentropic efficiency	87.32%	87.46%	0.16%

3.4 Body Force Model Calibration

Following the completion of required user input, automated model calibration commences.

3.4.1 Incorporation of User-Provided Body Force Grid

The first automated step in the system is the input of the user's body force grid. A flow chart depicting the high-level process conducted during this step in the automated procedure can be seen in Figure 3-6.

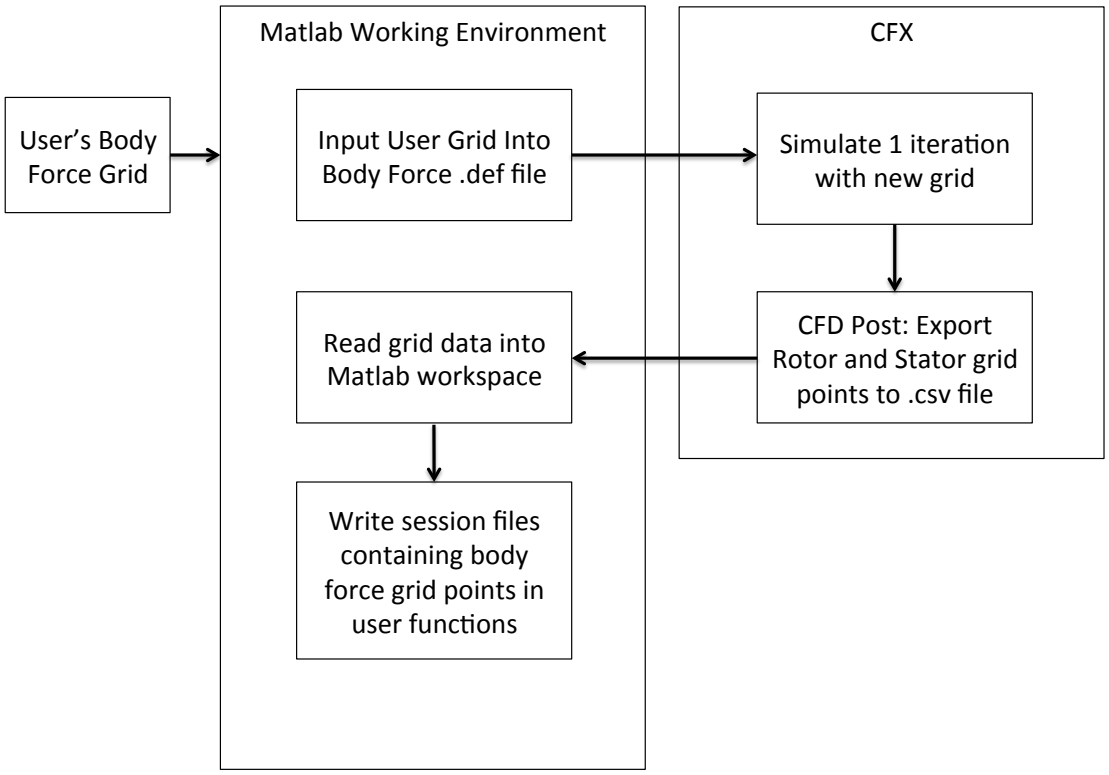

Figure 3-6: Flow chart depicting the incorporation of the user's body force grid.

A CFX-Pre session file is used to read the grid into a provided CFX .def file; the grid should be in ".grd" format. The name corresponding with the inlet boundary should be "Inlet," the outlet boundary should be named "Outlet," and the rotor and stator domains should be named "Rotor" and "Stator," respectively. Prior to beginning the model calibration process, the body force grid points must be known to avoid interpolation within the CFX user functions to maximize accuracy. User functions within CFX allow for the specification of data at points within the computational domain (a spatial look-up table). Matching the circumferentially averaged flow angles

(detailed in Section 2.1) is conducted at the specific points in the computational domain corresponding with the body force grid points, which is why accurate knowledge of these points is needed. A flow simulation on the body force grid, with no model present for the blade rows (so, an empty duct) is run for one iteration to initialize the axial and radial coordinates of the body force grid points in the results file that is needed for post-processing of the single-passage computations. A CFD-Post session file writes the coordinates of the grid points to a ".csv" file, which is then read into the Matlab script responsible for the automation. CFX-Pre and CFD-Post session files are then created using Matlab's "fprintf" command by appending the body force grid points to an already existing segment of the session files. These CFD-Post session files are responsible for the extraction of the single passage circumferentially averaged flow angles, body force circumferentially average flow angles, and the body force model's compressibility correction (ϵ) at the specific body force grid points. The CFX-Pre session file is used to input the newest version of the compressibility correction at the correct spatial location during model calibration iterations.

3.4.2 Generation of Blade Geometry Fields for Each Blade Row

The 3D blade data corresponding with the single passage geometry is used to generate blade geometry fields, a required input for the body force computations. The axial and radial coordinates, as well as the corresponding local blade mean camber angle from the meridional direction (κ) are needed. The format of the data for the rotor required to be provided by the user is as follows: the axial coordinate should be stored in a variable named "x_r" and provided in metres, the radial coordinate should be in a variable named "r_r" and provided in metres, and the local blade mean camber angle should be in a variable named "kappa_r" and provided in degrees. These three sets of data should be compiled in a Matlab ".mat" file, and stored in the working directory of the automation script. The format of the data for the stator being provided by the user is as follows: the axial coordinate should be in a variable named

"x_s" and provided in metres, the radial coordinate should be in a variable named "r_s" and provided in metres, and the local blade mean camber angle should be in a variable named "kappa_s" and provided in degrees. These three sets of data should be compiled in a Matlab ".mat" file, and stored in the working directory of the automation script. The local blade mean camber angle is defined to be negative in the direction of rotor rotation and positive opposite the direction of rotor rotation (so generally in the rotor the angles will be positive while in the stator they will generally be negative). The schematic found in Figure 3-7 illustrates positive and negative blade mean camber angle conventions.

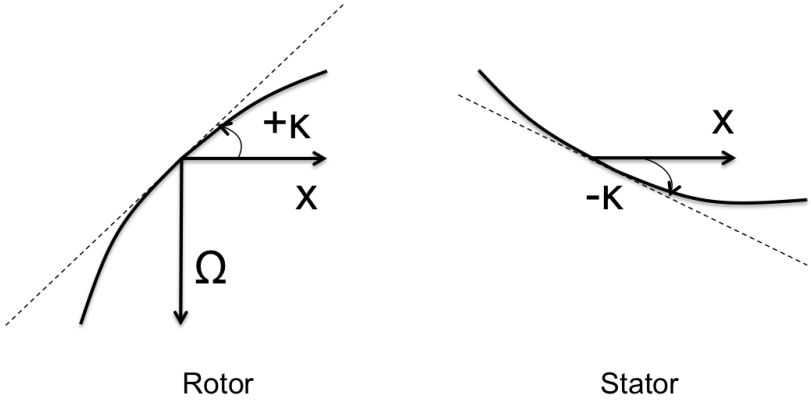

Figure 3-7: Single stage schematic displaying positive and negative blade mean camber angles.

This data is then interpolated onto the body force grid points within the script responsible for the automation procedure via Matlab's "scatteredInterpolant" function. The blade mean camber angle along with its axial and radial coordinates are used to create the interpolant function, and the body force grid points' axial and radial coordinates are used as the query points for the interpolation. Linear interpolation is used. The interpolated data is used to create fields for κ, σ, h, κ_{TE}, and κ_{LE} for each blade row, where κ_{TE}, and κ_{LE} are the blade mean camber angle at trailing edge and leading edge respectively. These fields are responsible for accurately modelling the turning force associated with the blade row as seen in Equation 2.9.

3.4.3 Single Passage Computations

Prior to commencing the body force model calibration, the data used for that calibration is needed. Thus single passage computations are conducted, in series, at all user-specified operating points. CFX-Pre session files are created using Matlab's "fprintf" command for the purpose of creating case definition .def files for all of the operating points chosen. The .def files are created using Matlab's "system" command to run the session files previously mentioned. The simulations are conducted via Matlab's "system" command by utilizing CFX's command line capabilities. This process starts at the operating point corresponding with the highest flow coefficient, and upon achieving a converged solution moves to the next operating point on the speedline (reducing flow coefficient). The results file from the most recently simulated operating point is used to initialize each of the remaining simulations to decrease computational cost.

CFD-Post session files are used to extract the circumferentially-averaged flow angles at all of the body force grid points (relative angles in rotor and absolute angles in stator), as well as the mass-weighted averaged total temperature ratio across the rotor at the peak isentropic efficiency operating point. The circumferentially-averaged flow angle data is written as a table with the following columns: the axial coordinate, the radial coordinate, and the corresponding flow angle. The total temperature ratio is written as a single number. Both of these sets of data are stored as .txt files within the working directory. This data is used for calibration of the turning force model, as outlined in Sections 3.4.5 and 3.4.6. CFD-Post session files are also used to extract rotor and stage isentropic efficiencies at all operating points. The rotor and stage isentropic efficiency are written as single numbers, and are stored as a .txt file within the working directory. This data is used for the optimization of the viscous force model, as outlined in Section 3.4.7.

3.4.4 Initial Body Force Computations

Turning force model calibration begins with a first body force simulation at the peak efficiency operating point with a simplified viscous force model present. The turning force model at this stage in the process is Hill's model without the compressibility correction (equivalent to Hall's model):

$$f_n = \frac{(\delta)\, W^2}{2r \cos \kappa / B}, \tag{3.3}$$

while the viscous force model at this stage in the process is expressed as

$$f_p = \frac{K_p^*}{h} \left(\overline{M}_{rel}^M \right)^2 W^2, \tag{3.4}$$

with W representing the relative velocity for the rotor. Note that in the stator's parallel force model, absolute velocity V is used instead of W. For the initial computation, an empirical guess for K_p^* is used, $K_p^* = 0.0145$ in the rotor and $K_p^* = 0.052$ in the stator. These empirical predictions were the final values discovered by Hill during his research [1]. The simulation is conducted in parallel across 3 cores. During system development, it was found that this level of parallelization produced the fastest results for the body force grid used. Flow angles (relative in rotor, absolute in stator) are computed from the results with a CFD-Post session file, and the difference from the corresponding single passage reported angles is computed within the session file using Perl commands. The difference is computed at all body force grid locations within the blade row(s), and sets the first version ϵ_1 of the compressibility offset correction ϵ.

$$\epsilon_{1,rotor}\left(x, r\right) = \beta_{SP}\left(x, r\right) - \beta_{BF}\left(x, r\right), \tag{3.5}$$

$$\epsilon_{1,stator}\left(x, r\right) = \alpha_{SP}\left(x, r\right) - \alpha_{BF}\left(x, r\right), \tag{3.6}$$

where $\beta_{SP}\left(x, r\right)$ is the relative circumferentially-averaged flow angle in the rotor reported from the single passage results, $\beta_{BF}\left(x, r\right)$ is the relative flow angle in the rotor

reported from the body force computation, $\alpha_{SP}(x,r)$ is the absolute circumferentially-averaged flow angle in the stator reported from the single passage results, and $\alpha_{BF}(x,r)$ is the absolute flow angle from the stator reported from the body force computation. The session file writes the compressibility correction data at all grid locations to a .txt file along with the axial and radial coordinates of the corresponding grid point, which is stored within the working directory. Within this same session file, the difference in isentropic rotor and stage efficiency η between the body force computation and the single passage results is used for a calculation of the update of the viscous force coefficient K_p^* in both the rotor and stator, respectively, which is written as a .txt file and stored within the working directory. The difference between the two efficiencies sets the value for a viscous force coefficient incorporated in the definition of the viscous force as seen in Equation 3.7. At this point in the process it is expected that the difference between the two efficiencies is small enough so that K_p^* will scale linearly:

$$K_p^* = \left(1 - \frac{\eta_{SP} - \eta_{BF}}{\eta_{SP}}\right) K^*_{p_{empirical}}. \tag{3.7}$$

Following the first iteration of K_p^*, the efficiency difference acts as a scaling factor on the previous K_p^* value, as seen in Equation 3.9.

3.4.5 Determining the Final Compressibility Correction ϵ

Once the first version of the compressibility correction and the calibrated viscous force coefficient are created, the working Matlab script responsible for the automated model development enters a "while" loop. A flow chart depicting the process conducted within this loop can be found in Figure 3-8.

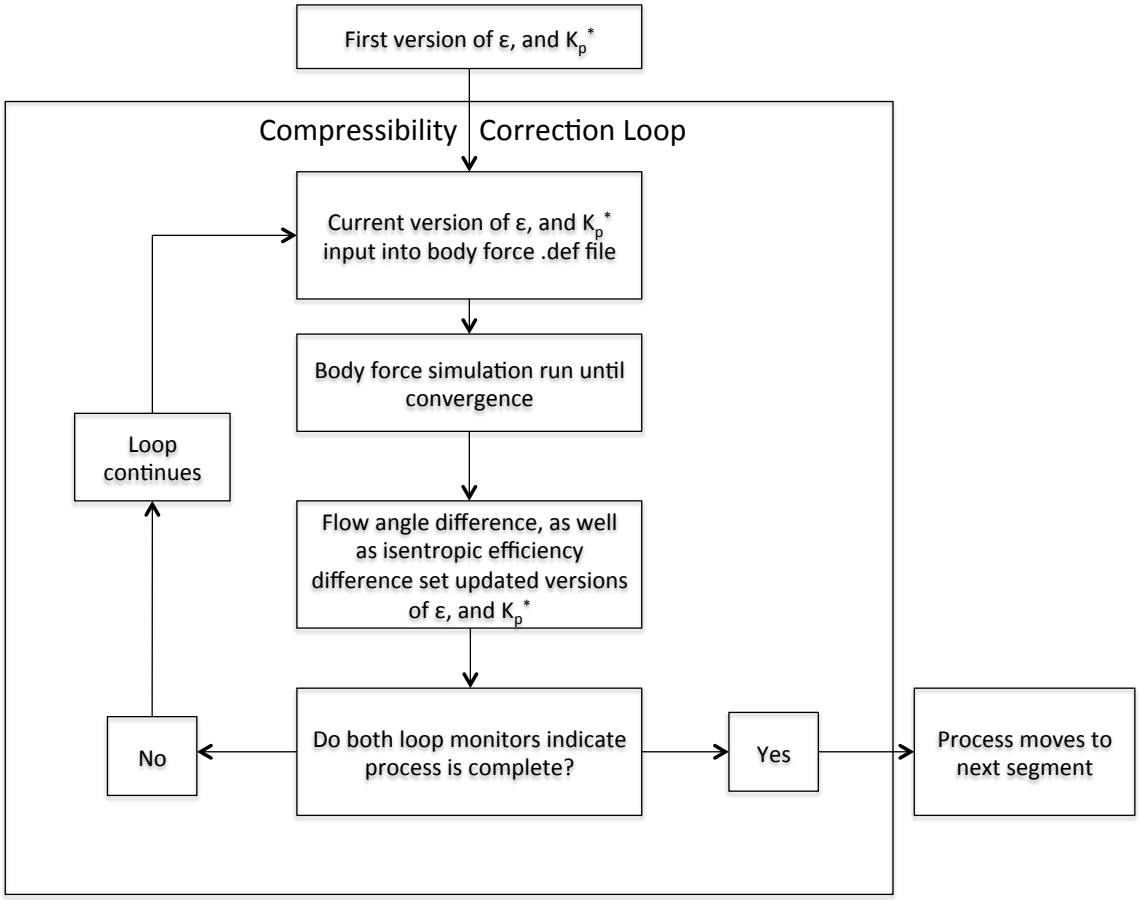

Figure 3-8: Flow chart depicting the compressibility correction loop.

To start, a CFX-Pre session file reads the .txt file pertaining to the current version of the compressibility correction fields ϵ_i and K_p^* (for the rotor and stator) via Perl scripting commands. The session file then inputs the data into the body force .def file via CCL. The simulation at the peak efficiency corrected mass flow is initialized from the most recent body force results file and run to convergence. The difference between the body force and single passage results is assessed within the same CFD-Post session file detailed in Section 3.4.4, and sets the updated versions of ϵ and K_p^* as follows:

$$\epsilon_{new}(x,r) = \epsilon_{old}(x,r) + \left[\beta_{SP}(x,r) - \beta_{BF}(x,r)\right] \tag{3.8}$$

$$K^*_{p,new} = \begin{cases} K^*_{p,old}\left(1 - C_{emp}\sqrt{\frac{\eta_{BF}-\eta_{SP}}{\eta_{SP}}}\right) & \text{if } \eta_{BF} \geq \eta_{SP} \\ K^*_{p,old}\left(1 + C_{emp}\sqrt{\frac{\eta_{SP}-\eta_{BF}}{\eta_{SP}}}\right) & \text{if } \eta_{SP} > \eta_{BF} \end{cases}, \tag{3.9}$$

where C_{emp} is an empirical scaling factor set to 0.225 and 0.45 for the rotor and stator, respectively. These values come from Hill's research, and are based on the iterative procedure he conducted while manually adjusting K^*_p [1]. As η_{BF} approaches η_{SP}, the adjustment of K^*_p based on the efficiency alone typically results in over-adjustment, thus C_{emp} is incorporated to reduce overshoot of K^*_p. The "while" loop implemented in Matlab repeats this process until monitors for the rate of change of both quantities determine that the model is converged. The details of these monitors $\mathcal{M}$ are as follows:

$$\mathcal{M}_\epsilon(x,r) = \left|\frac{\epsilon_i(x,r)}{\epsilon_{i-1}(x,r)}\right| - 1 \tag{3.10}$$

$$\mathcal{M}_{K_p} = \frac{|\eta_{SP} - \eta_{BF}|}{\eta_{SP}}. \tag{3.11}$$

The compressibility correction monitor is evaluated at all body force grid points, and the maximum value is used for the final assessment. Convergence is achieved when both of these monitors fall below 0.01. This value is chosen as it signifies that the body force model is within 1% agreement with the single passage isentropic efficiency results, which is deemed sufficiently accurate by the author. For the compressibility correction, this represents a maximum change at all body force grid points of 1%, suggesting the flow angles are sufficiently matched.

3.4.6 Rotor Blade Recambering

Following the convergence of the compressibility correction loop, the model for the turning force is partially complete. As outlined in Section 2.1, the matching of flow angles ensures the leading edge incidence of the blades is accurately modelled, however this does not ensure the trailing edge work input is correct. To accurately capture

the trailing edge work input, the model incorporates Hill's recambering process [1]. Prior to commencing this process, a CFD-Post session file is used to extract the mass-averaged total temperature ratio across the rotor (τ) from the body force computation result responsible for terminating the compressibility correction loop. The difference between the body force and single passage result for this total temperature ratio sets the first version of a design constant to begin the rotor blade recambering process. The first version of the recambering constant scales linearly with an empirical recambering constant of $\Lambda_{empirical} = 0.27$, which was the version of the constant found by Hill during his research [1].

$$\Lambda = \left(\frac{\tau_{NAT}}{\tau_{SP}}\right) \Lambda_{empircal} \tag{3.12}$$

A "while" loop implemented in the Matlab script responsible for model calibration starts by using a CFX-Pre session file to input the current version of the recambering design constant into the body force .def file. This affects the blade camber distribution as follows:

$$\kappa_{new}(x,r) = \kappa_{old}(x,r) + \Lambda_{recamber} \frac{(x - x_{LE}(r))}{(x_{TE}(r) - x_{LE}(r))} (\beta_{TE,SP}(r) - \beta_{LE,SP}(r)), \tag{3.13}$$

where $\kappa_{new}(x,r)$ is the new blade camber profile at each rotor grid point. A schematic produced by Hill details the effect of recambering [1], and can be seen in Figure 3-9.

Typically the blade loading is highest in the first quarter chord of the rotor blade, thus the recambering is performed linearly from leading edge to trailing edge, meaning that the camberline is unaltered at the leading edge. By linearly recambering, the body force camberline is a combination of correct swirl angle at the leading edge and correct swirl velocity at the trailing edge. To produce the recambered blade, changes in relative flow angle from leading edge to trailing edge are extracted from single passage RANS and are used to radially scale the re-cambering, as seen in Equation 3.13 represented by the $(\beta_{TE,SP}(r) - \beta_{LE,SP}(r))$ term. By doing this, the spanwise total temperature profile at the rotor exit is preserved once the converged value of Λ is

obtained. Following the input of the recamber constant, the first recamber simulation is initialized by the most recent body force results file and run to convergence. A CFD-Post session file extracts the total temperature ratio previously discussed and this is used to compute a new value of the recambering constant as follows:

$$\Lambda_{new} = \begin{cases} \Lambda_{old}\left(1 - \sqrt{1 - \frac{\tau_{BF}}{\tau_{SP}}}\right) & if\ \tau_{SP} \geq \tau_{BF} \\ \Lambda_{old}\left(1 + \sqrt{\frac{\tau_{BF}}{\tau_{SP}} - 1}\right) & if\ \tau_{BF} > \tau_{SP} \end{cases}. \tag{3.14}$$

In a similar manner to the compressibility correction loop, the recambering loop makes use of a convergence monitor. The details of the monitor is as follows:

$$\mathcal{M}_{recamber} = \left|1 - \frac{\tau_{BF}}{\tau_{SP}}\right|. \tag{3.15}$$

The monitor terminates the loop if the calculation results in a value equal to or less than 0.01. This value is chosen as it signifies that the body force model is within 1% agreement with the single passage rotor total temperature ratio, which is deemed sufficiently accurate by the author. The convergence of this loop marks the completion of the normal force model development.

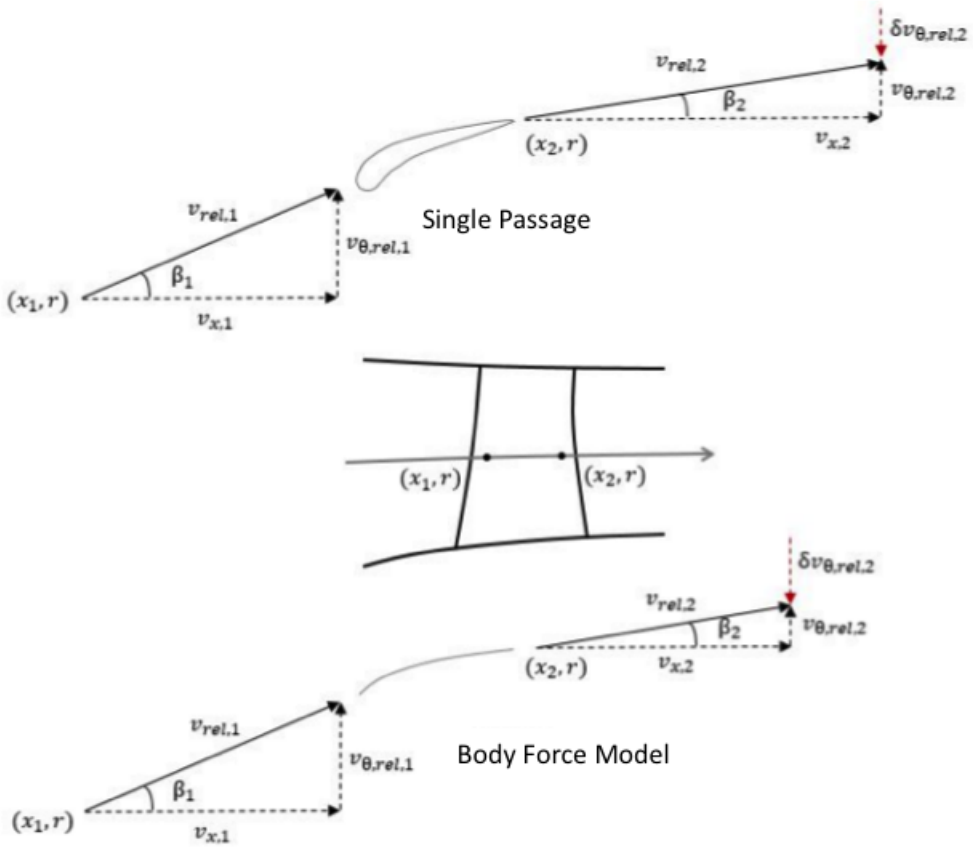

Figure 3-9: Mismatched swirl velocity with a constrained flow angle due to absence of blockage [1]. Used with permission.

3.4.7 Viscous Force Coefficient Optimization

With the normal force model complete, the automation scheme begins the calibration of the parallel force model. The parallel force model used in this thesis is a modified version of Hill's model [1], which can be found in Equation 2.11. The form of the viscous force model used in this work can be seen in Equation 3.16.

$$f_p = \begin{cases} \frac{K_{p1}}{h}\left[\left(\overline{M}_{rel}^{M}\right)^2 + K_{p2}\left(\overline{M}_{rel}^{M} - M_{ref}\right)^2\right] W^2 & \text{if } \overline{M}_{rel}^{M} \leq \overline{M}_{rel,\text{ peak }\eta}^{M} \\ \frac{K'_{p1}}{h}\left[\left(\overline{M}_{rel}^{M}\right)^2 + K'_{p2}\left(\overline{M}_{rel}^{M} - M'_{ref}\right)^2\right] W^2 & \text{if } \overline{M}_{rel}^{M} > \overline{M}_{rel,\text{ peak }\eta}^{M} \end{cases}, \quad (3.16)$$

where the primed coefficients denote the viscous coefficients used above the peak efficiency point, and the non-primed coefficients are used below the peak efficiency point. In isolating the parallel force model above the peak efficiency point from the model below the peak efficiency point, the two models can be solved for simultaneously, as the coefficients are independent. As mentioned in Section 2.1, typically the coefficients K_{p1}, K_{p2}, and M_{ref} are adjusted in attempts to match the efficiencies reported by the model at all operating points along the speedline. However, in this automated model calibration, the viscous force coefficients are subjected to a Nelder-Mead optimization procedure implemented in Matlab via the "fminsearch" algorithm. The process is illustrated in Figure 3-10.

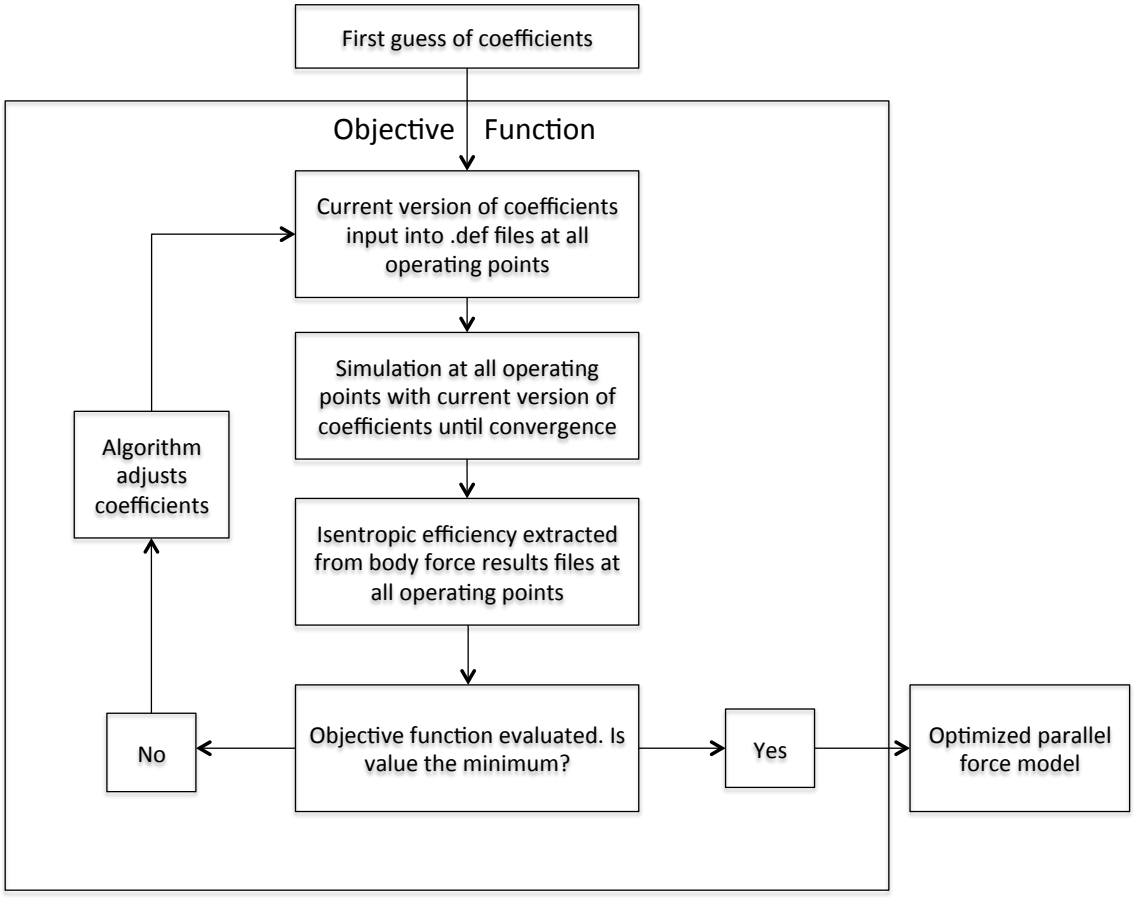

Figure 3-10: Process conducted during optimization of parallel force model coefficients at flow coefficients either above or below peak efficiency.

The objective function for the optimization process is

$$\mathcal{F}_{obj} = \sqrt{\frac{\sum_{i=1}^{n} \left(\eta_{SP} - \eta_{BF}\right)^2}{n}}, \tag{3.17}$$

where n is the number of operating points (including peak efficiency) on a given side of peak efficiency. The objective function for the rotor is the RMS error between body force and single passage reported rotor isentropic efficiency, while the stator's objective function is the RMS error of the stage isentropic efficiency. Because the rotor has a direct effect on the stage efficiency, it is important to optimize the model for the rotor prior to that of the stator. The completion of the previously conducted compressibility correction loop indicates that the simplified f_p at the peak efficiency operating point corresponds with sufficient agreement between the single passage and body force isentropic efficiences. Rearranging Equation 3.4 leads to

$$K_p^* = \frac{f_p}{\left(\overline{M}_{rel}^M\right)^2 W^2} h. \tag{3.18}$$

Rearranging Equation 3.16 leads to K_{p1} expressed as

$$K_{p1} = \frac{f_p}{\left[\left(\overline{M}_{rel}^M\right)^2 + K_{p2}\left(\overline{M}_{rel}^M - M_{ref}\right)^2\right] W^2} h, \tag{3.19}$$

effectively reducing the number of independent variables from 3 to 2 (K_{p2} and M_{ref}). The first guess for M_{ref} is simply $\overline{M}_{rel}^M$, which is consistent with the first guess Hill employed during his study [1]. This reduces Equation 3.19 to

$$K_{p1} = \frac{f_p}{\left[\left(\overline{M}_{rel}^M\right)^2\right] W^2} h = K_p^* \tag{3.20}$$

A CFD-Post session file is used to extract K_p^* from the body force results file upon termination of the recambering loop. The first guess for K_{p2} is empirical, based on

the ratio of Hill's final versions of K_{p1} and K_{p2} to set the guess as

$$K_{p2} = 40000 K_{p1}. \tag{3.21}$$

Upon being subjected to the first guess

$$\vec{x}_o = [K_{p2}\ M_{ref}], \tag{3.22}$$

the "fminsearch" algorithm creates a simplex around this guess by adding 5% to each component of $\vec{x}_0$ to create two new vectors. The algorithm uses these two new vectors as elements of the simplex, along with the first guess. Then, the algorithm modifies the simplex repeatedly with either a reflect, contract, expand, or shrink step until it converges on the minimum. The full details of the "fminsearch" algorithm can be found in Ref. [15]. A visualization of the Nelder-Mead process utilizing a triangle simplex for a two variable optimization is found in Figure 3-11.

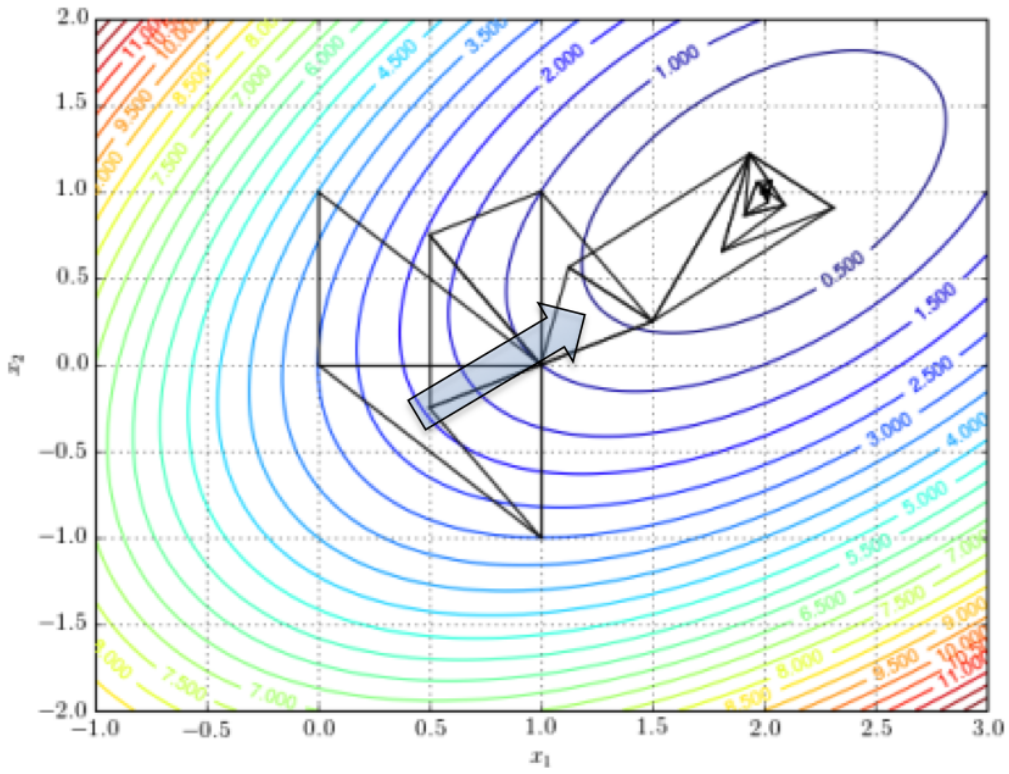

Figure 3-11: Example Nelder-Mead process for two variable optimization [21].

Following the first guess, the main script calls a second instance of Matlab. The two scripts run in parallel to simultaneously solve the optimization problems above and below the peak efficiency point. The two optimizations are independent and are carried out in parallel to reduce the time required for model calibration. The system optimizes the rotor coefficients first, and upon completion, optimizes the stator coefficients using the same approach.

The Matlab function file responsible for the optimization uses a CFX-Pre session file to input the current version of the viscous force coefficients into the CFX case definition file at all operating points. Each loop of the optimization starts by writing the session file responsible for the input of the coefficients via Matlab's "fprintf" command. These points are then simulated in series, beginning at the highest flow coefficient operating point, while moving along the speedline by reducing the flow coefficient. The simulations are initialized by the most recent results file at the

corresponding operating point. Upon reaching a converged solution, a CFD-Post session file extracts the relevant isentropic efficiency, and writes the value of the efficiency to a .txt file stored within the working directory. Once the efficiency at all operating points is obtained, the values are read into the working directory and the objective function is evaluated. Each iteration of the optimization procedure records the version of the coefficients being optimized, as well as the corresponding value of the objective function into a plain text file so that convergence can be externally monitored. Before moving to the next iteration of the optimization procedure, the optimization below the peak efficiency reads the latest version of the viscous force coefficients above peak efficiency, and inputs these into the body force .def file below peak. The same is done vice-versa above the peak efficiency point, to ensure that upon completion, the model is complete (both above and below peak efficiency point coefficients will be correct). A visual representation of the exchange of coefficients between the above and below peak efficiency optimization procedures is presented in Figure 3-12.

Employing the approach outlined in this chapter results in automated calibration of a body force model for a fan or compressor stage. The resultant model and the results produced by the model for NASA stage 67 are discussed in detail next.

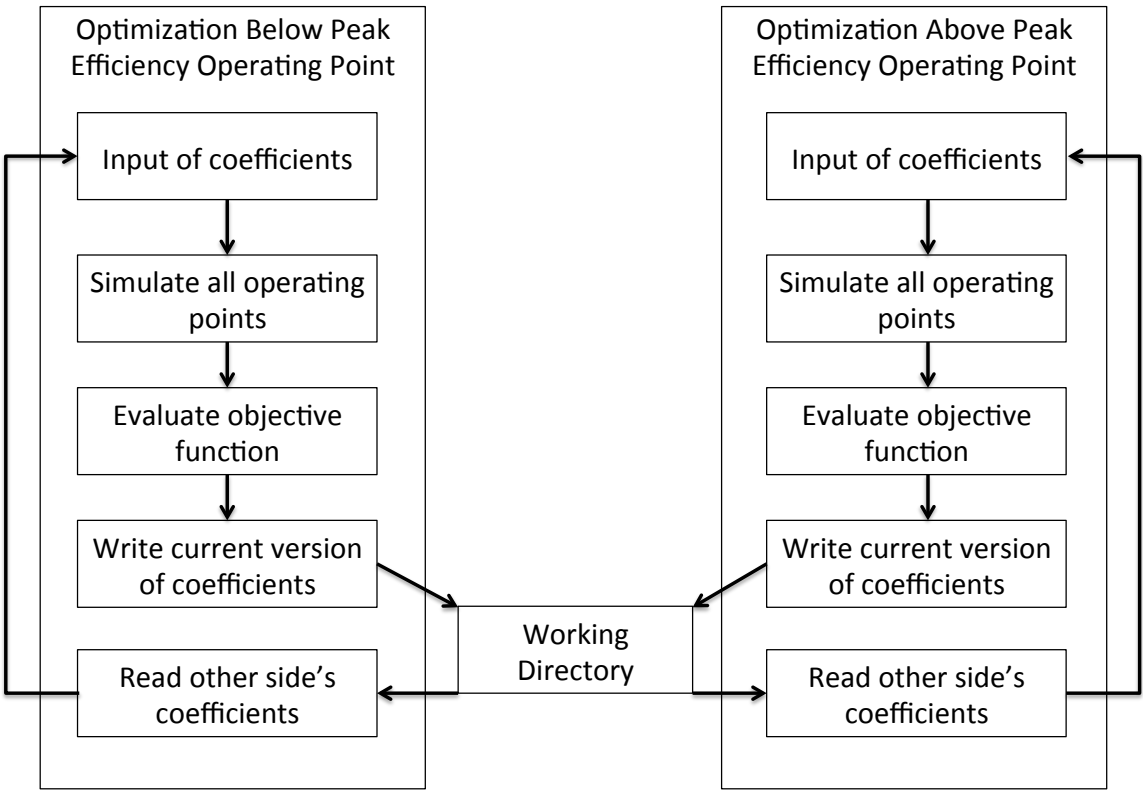

Figure 3-12: Exchanging of coefficients between parallel optimization processes.

Chapter 4

Body Force Model Assessment

In this chapter, the body force model produced by the automated system for NASA stage 67 at 90% corrected design speed is detailed. The model's performance is assessed with comparison to single passage results, as well as the results produced by Hill's manually generated body force model [1]. The results of the viscous force optimization for both the rotor and stator is presented, as well as the associated computational cost of model calibration.

4.1 Normal Force and Peak-Efficiency Viscous Force Model

The system presented in this work proves capable of calibrating a normal force model, with performance on par with a user-generated model. The modelling constants obtained during normal force model calibration and the number of iterations conducted to determine them are shown in Table 4.1, which includes the simplified parallel force model constants described in Section 3.4.5,

Table 4.1: Outputs of the normal force and peak-efficiency viscous force model calibration.

	$K^*_{p,rotor}$	$K^*_{p,stator}$	Λ
Constant	0.0209	0.109	0.204
# of Iterations	22		2

At the peak efficiency mass flow rate, 31.1 kg/s (flow coefficient $\phi = 0.5$ based on midspan blade speed), the relevant results produced by the normal force model are outlined in Table 4.2. The model's results are compared with the single passage counterparts, and the results produced by Hill's work [1], with the error calculated relative to the single passage results.

Table 4.2: Automated model versus single passage and Hill's model.

	single passage	automated model	% error	Hill's model	% error
$\dot{m}_{corr}$ (kg/s)	31.1	31.1		31.1	
η_{is}(rotor, %)	92.5	93.2	0.75	92.4	0.10
η_{is}(stator, %)	89.3	90.1	0.84	90.0	0.79
$\tau_{rotor} - 1$	0.1291	0.1294	0.23	0.1314	1.78

The agreement between the automated model and the single passage results is on par with Hill's results, except for the rotor isentropic efficiency. This can be attributed to the monitor responsible for $K^*_{p,rotor}$, seen in Equation 3.11, as the percent error fell below the 1% threshold corresponding with loop convergence. If the user of the automated system desired a stronger agreement, adjusting the convergence criteria accordingly for Equation 3.11 would accomplish this.

The final version of the compressibility correction, ϵ, is obtained in the same loop used to determine, K^*_p, as outlined in Subsection 3.4.5. Hill's model required 19 iterations to obtain the final spatial ϵ field [1], whereas the automated model conducted 22 iterations to accomplish the same task. A comparison of the difference in flow angles between the model and single passage results can be found in Figure

4-1. This figure indicates that the automated model produces stronger matching between the single passage and body force reported flow angles than does the user-calibrated approach. As mentioned in Section 3.4.5, the process of determining the compressibility correction, ϵ, involves observing the change in ϵ between each iteration. This result suggests that the convergence criteria for the compressibility correction monitor, Equation 3.10, is more precise than the traditional manual method.

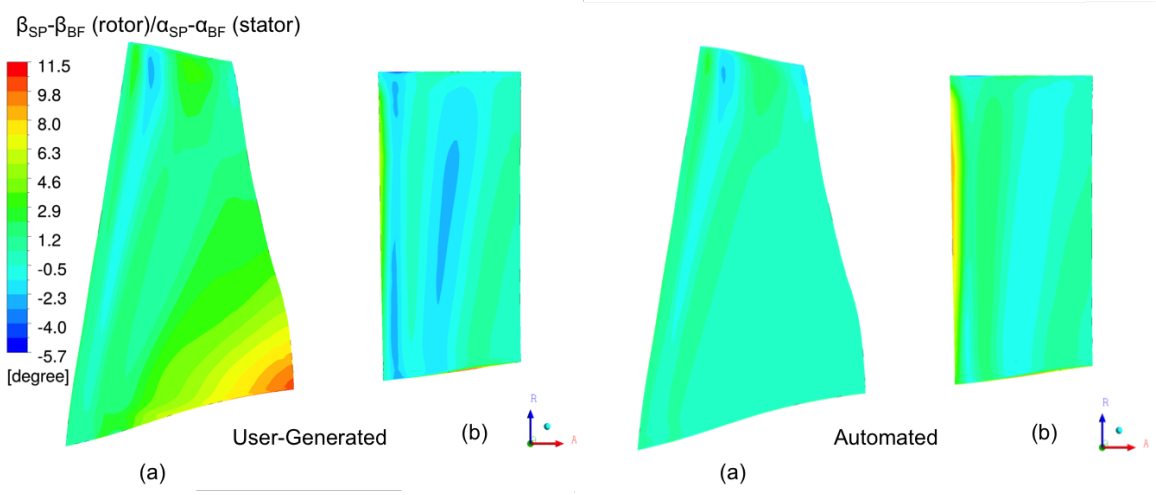

Figure 4-1: Automated model versus user-generated model for flow angle deviation from single passage. (a): rotor; (b): stator.

The agreement of the key metrics for the peak-efficiency performance suggest that the compressibility correction and rotor recambering accurately capture the blade loading; however, as seen in Figure 4-2, where the leading edge nears the casing there is an overprediction of the work input. Following this, the gradient of work production flips directions to ensure the work being predicted is accurate at the trailing edge. Thus the model's chordwise loading prediction is inaccurate and is introducing non-physical effects. Suggested practices to avoid this in future implementations are discussed in Section 5.3.

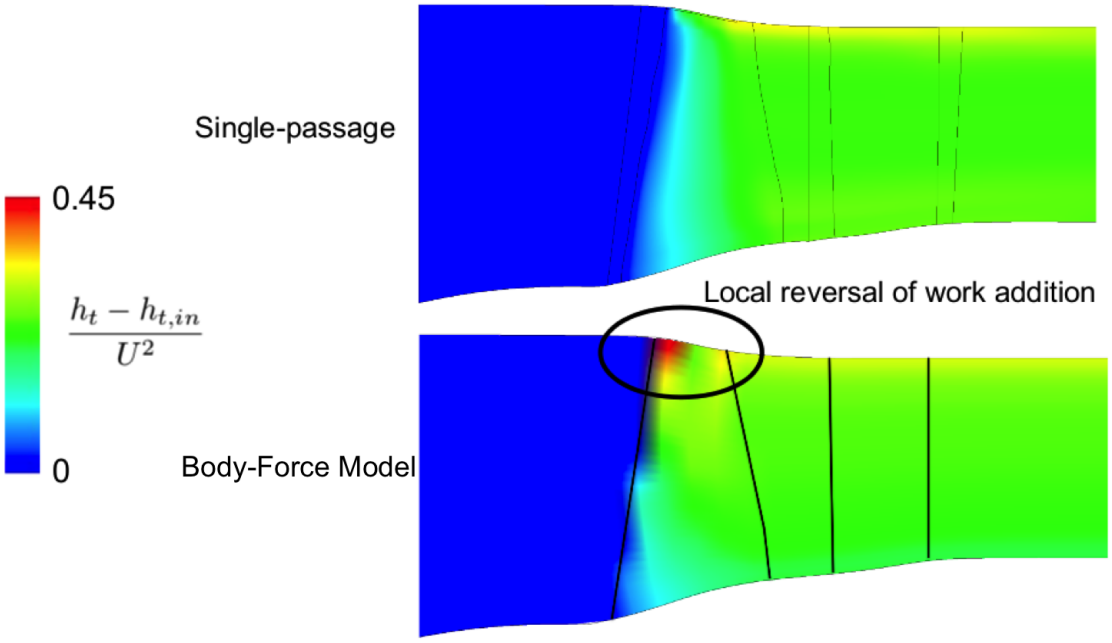

Figure 4-2: Comparison of work coefficient between single passage and body force results.

4.2 Viscous Force Coefficient Optimization

The operating points chosen for this study are outlined in Table 4.3. These points were chosen as they correspond with evenly distributed locations on the speedline being simulated, centred around the peak efficiency operating point of 31.1 kg/s.

Table 4.3: Operating points used during optimization procedure.

Operating Point	1	2	3	4	5	6	7
$\dot{m}_{corr}$ (kg/s)	28.7	29.5	30.3	31.1	31.9	32.7	33.5
ϕ	0.461	0.474	0.487	0.5	0.513	0.526	0.539

As mentioned in Section 3.4.7, the rotor optimization is conducted first to ensure the stage optimization exclusively targets the stator's effect on the stage efficiency. The viscous force model coefficients produced by the optimization procedure for the rotor can be found in Table 4.4. Both procedures (above and below peak efficiency)

required 41 iterations of the Nelder-Mead optimization algorithm, and the convergence history of the objective function can be found in Figure 4-3. The RMS error minima determined for the rotor optimization procedure is 0.0099 and 0.0017 for below and above peak respectively.

Table 4.4: Viscous force coefficients produced by Nelder-Mead optimization for the rotor.

Below Peak		Above Peak	
K_{p1}	0.003467	K'_{p1}	0.01157
K_{p2}	660.5	K'_{p2}	662.5
M_{ref}	1.061	M'_{ref}	0.9620
$\overline{M}^{M}_{rel,\ \text{peak}\ \eta}$	0.9870	$\overline{M}^{M}_{rel,\ \text{peak}\ \eta}$	0.9870

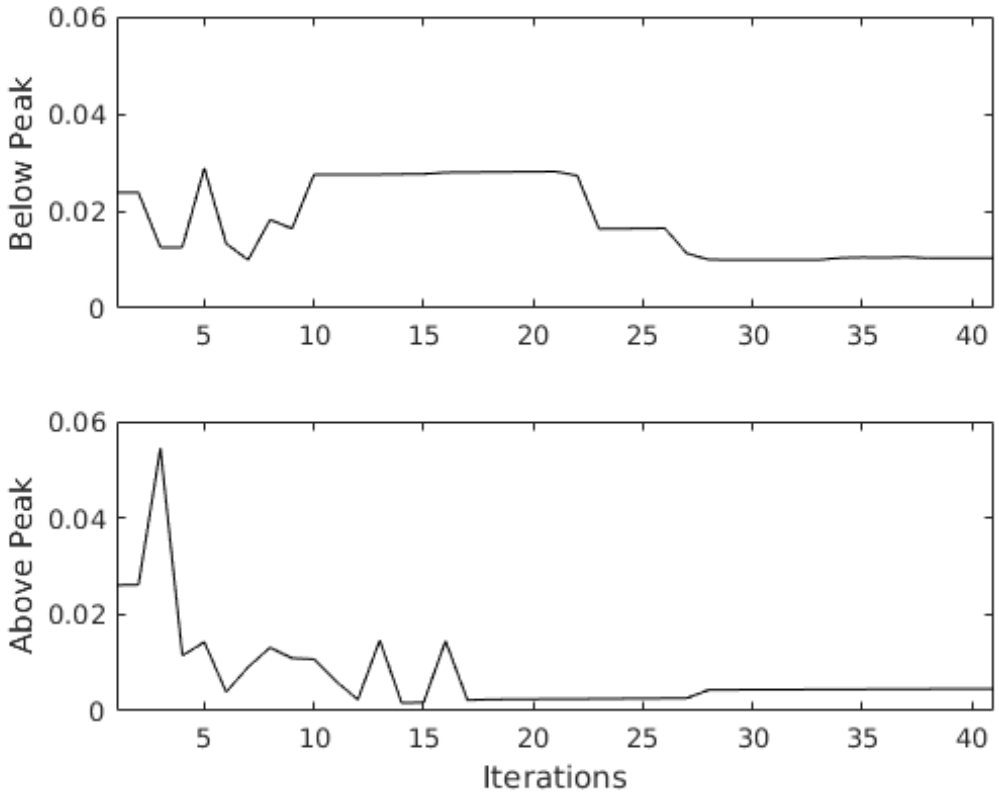

Figure 4-3: Objective function history for rotor viscous force coefficients optimization.

Following the completion of the rotor's viscous force coefficient optimization, the

stator's viscous force coefficients are optimized in an identical manner. The coefficients produced by the Nelder-Mead optimization can be found in Table 4.5. These coefficients were obtained following 27 and 32 iterations for below and above the peak efficiency point respectively, and the convergence history for the optimization process can be found in Figure 4-4. The RMS error minima determined for the stator optimization procedure is 0.0517 and 0.0897 for below and above the peak efficiency point respectively. Comparing these minima with those found for the rotor's optimization process suggests that the stage efficiency may not be the most suitable parameter to calibrate the stator's viscous force model. Further discussion of this finding can be found in Section 5.3.

Table 4.5: Viscous force coefficients produced by Nelder-Mead optimization for the stator.

Below Peak		Above Peak	
K_{p1}	0.00108	K'_{p1}	0.05062
K_{p2}	12.92	K'_{p2}	5.606
M_{ref}	1.761	M'_{ref}	0.6492
$\overline{M}^{M}_{rel,\ \text{peak}\ \eta}$	0.6045	$\overline{M}^{M}_{rel,\ \text{peak}\ \eta}$	0.6045

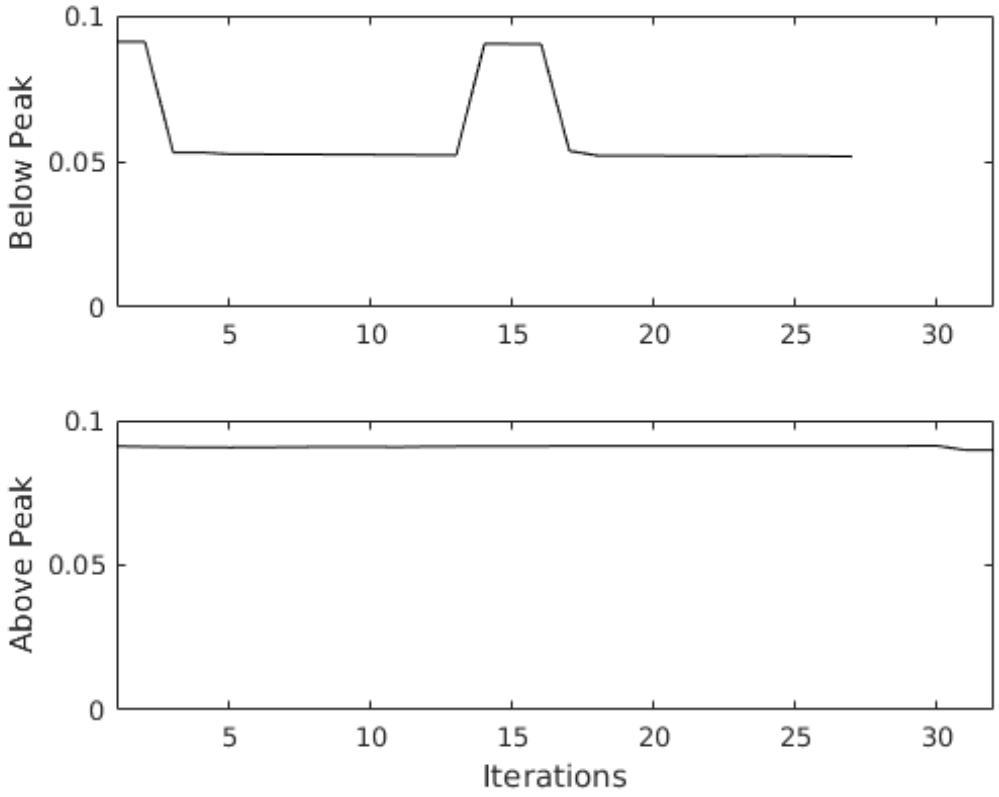

Figure 4-4: Objective function history of stator viscous force coefficients optimization.

The efficiency as a function of flow coefficient produced by the model is compared with the single passage results used for calibration in Figure 4-5. As the RMS error minima suggests, the stator's viscous force model does not produce the same level of agreement as the rotor's viscous force model. The model is unable to match the steep decline in stage efficiency as the operating conditions move away from the peak efficiency operating point. The isentropic efficiencies produced by the body force model are compared at each operating condition to the single passage result used for calibration in Table 4.6. The model predicts the rotor isentropic efficiency sufficiently well, with the highest error being 1.32%, and the smallest being 0.10%. The model is unable to match the single passage results in its prediction of the stage efficiency, with especially poor performance as the operating conditions move further away from the peak efficiency. The "flat" behaviour seen in Figure 4-4 suggests that the sensitivity of the stage efficiency with regards to the adjustment of the stator's viscous force

coefficients is low in comparison to the rotor results. The single passage results at the two highest mass flows are nearing choke conditions, and the lack of blade metal blockage in the body force model becomes more significant, as the results in Table 4.6 suggest. Possible solutions are outlined in Section 5.3.

Table 4.6: Body force reported isentropic efficiencies versus single passage result.

$\dot{m}_{corr}$ (kg/s)	28.7	29.5	30.3	31.1	31.9	32.7	33.5
$\eta_{rotor,BF}$ (%)	89.4	91.1	92.3	92.7	91.5	88.9	84.3
$\eta_{rotor,SP}$ (%)	89.0	90.0	91.2	92.5	91.7	88.8	84.2
% error	0.506	1.16	1.32	0.227	0.240	0.101	0.131
$\eta_{stage,BF}$ (%)	86.0	88.3	90.4	90.6	88.9	85.7	80.1
$\eta_{stage,SP}$ (%)	77.7	82.8	88.0	89.3	87.9	77.3	64.4
% error	10.7	6.62	2.81	1.37	1.16	10.9	24.4

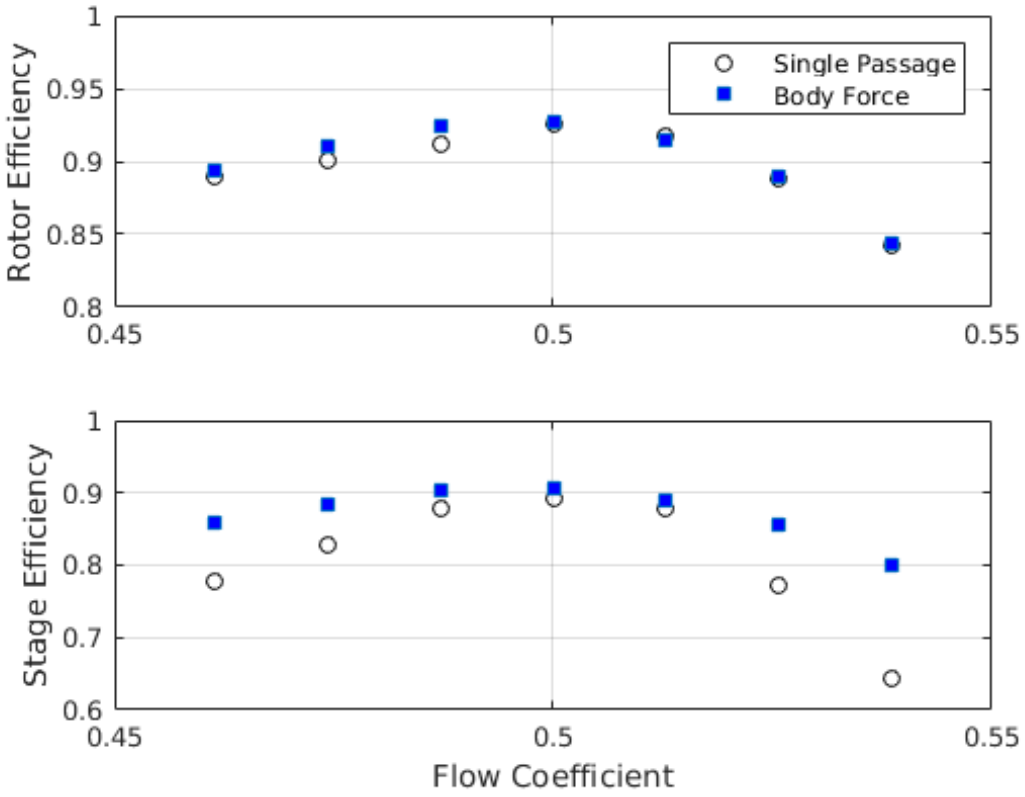

Figure 4-5: Body force speedline of isentropic rotor and stage efficiency compared with single passage results.

For a body force model to accurately capture the effects of an inlet distortion, the model's prediction of off-design performance must also match the level of agreement at design. To assess the model's capability, the rotor total temperature ratio, rotor total pressure ratio, and stage total pressure ratio are plotted versus flow coefficient in Figure 4-6 at the operating points indicated in Table 4.3. The agreement between the automated model and the single passage computations is on par with Hill's user generated model [1] for all three metrics until approaching choke conditions. This is to be expected, as blade metal blockage is not modelled, resulting in choking effects being significantly delayed. These off-design results bode well, and it is determined that the body force model is sufficiently calibrated to serve as an inflow distortion study tool, a suitable alternative to full-wheel URANS simulations.

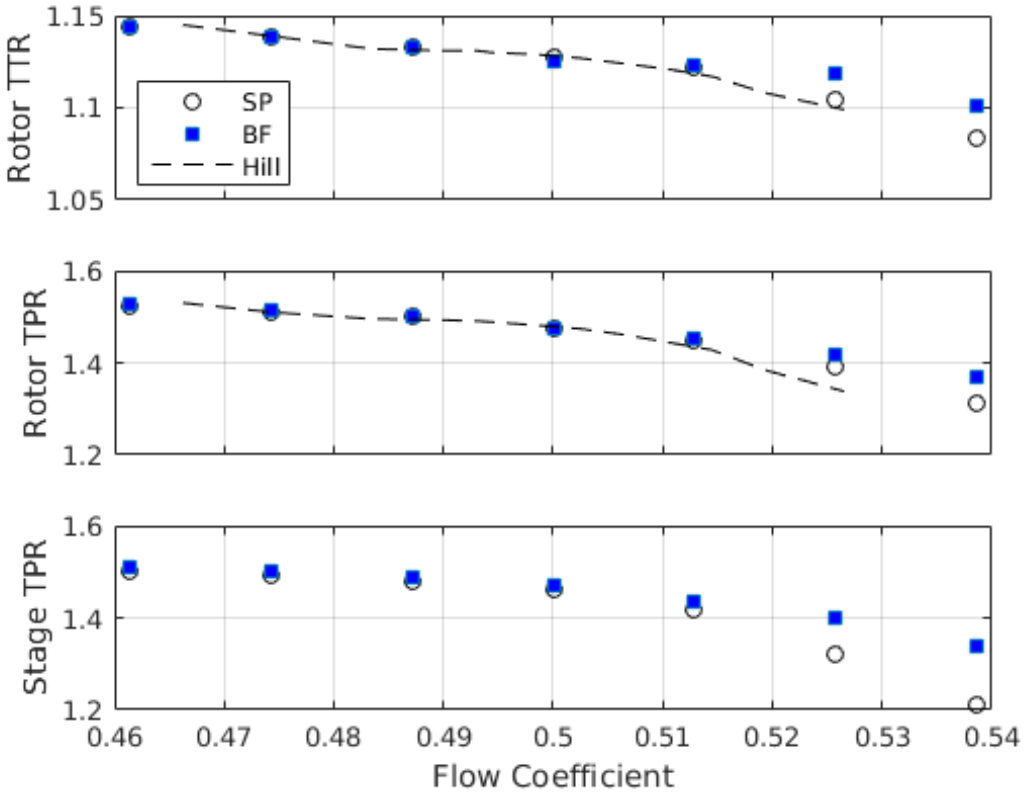

Figure 4-6: Rotor total temperature ratio, total pressure ratio, and stage total pressure ratio at off-design conditions.

4.3 Computational Cost

Model calibration requires numerous iterations for each step of the process. The computational cost of each step is outlined in Table 4.7, with the computational time being presented in terms of core-days. Model calibration was conducted on an Advanced Clustering Technologies MicroHPC^{2}Workstation [21], which contains two Intel Six Core Xeon E5-2603v4 1.7 GHz processors. Computations were conducted in parallel across three cores, as this level of parallelization was found to produce results in the least time for the body force grid used in this study. Recall that the optimizations above and below peak efficiency are conducted in parallel. The computational time associated with the stator optimization is one order of magnitude smaller than the time required for the rotor optimization process. The reason for this

is that the simulations conducted during stator optimization converged quickly as the coefficients were changing minimally between iterations.

Table 4.7: Computational time required for model development; computations on 3 cores @ 1.7 GHz.

Step of Model Calibration	# of Iterations	Computational Time (core-days)
Compressibility Correction ϵ	22	11.5
Rotor Recambering	2	0.5
Rotor Optimization Below Peak	41	10.0
Rotor Optimization Above Peak	41	10.0
Stator Optimization Below Peak	27	1.0
Stator Optimization Above Peak	32	1.0
Full Model Development		23.0

Traditional full-annulus URANS comutational grids can be in excess of 100 million cells, and require anywhere from 20-30 rotor revolutions to reach a converged solution. One of these computations can take in excess of two months [19, 22]. The advantage of the body force model becomes apparent when applying the model to a variety of inlet distortion cases, as the computational time associated with achieving a URANS converged computation is approximately 2 orders of magnitude greater than that of a body force model once it is calibrated.

Chapter 5

Conclusions and Future Work

In this thesis, an automated system is presented for the purpose of calibrating a body force model for a single stage compressor. In this chapter, a summary of the work conducted, the key findings of the study, and recommendations for future work are discussed.

5.1 Summary

In the past, several authors have conducted studies on the development of body force models and assessed those models' accuracy. Multiple applications of expert systems, as well as Nelder-Mead optimization procedures have been conducted in previous work; however, none of them incorporate all of these ideas at once. The lack of an existing automated system capable of producing an optimized body force model is the motivation behind the work in this thesis.

The automated system requires user inputs of the peak efficiency corrected mass flow rate, the corrected speed of the machine, single passage CFX definition files (with accompanying geometry), the operating points of the speedline, and the user-generated body force grid. Following the user input, model calibration begins with single passage RANS simulations at all design points specified to extract the calibration data for the model. The turning force model, which is an adaptation of Hall's model by Hill, is the first focus during calibration. The viscous loss model is an

adaptation of Peters' model, applying two unique instances of the model on either side of the peak efficiency point. The automated system is implemented in Matlab, using CFX-Pre and CFD-Post session files for data input and output respectively.

The model is able to produce results at the peak efficiency operating point to within 1% of the single passage results for both work input and efficiency. At this operating condition, the automated model performs almost identically to a user-generated model produced in Hill's work. The portion of the normal force model calibration that determines the compressibility correction results in non-physical work removal near the casing-leading edge region of the rotor. The minima found for the rotor's viscous force objective function during optimization are 0.0099 and 0.0017 for the below and above peak efficiency point respectively; the minima found for the stator's viscous force objective function during optimization are 0.0517 and 0.0897 for the below and above peak, efficiency point, respectively. The flat behaviour seen in Figure 4-4 indicates that the adjustment of the parallel force coefficients results in minimal change in the isentropic stage efficiency produced by the model. This suggests that the stage isentropic efficiency is not the most suitable parameter used to calibrate the stator's parallel force model; alternative parameters are outlined in Section 5.3. Despite this finding, the model produced performs suitably at off-design conditions not pertaining to choke conditions, predicting the rotor total pressure ratio and total temperature ratio to within 0.4% and 0.2% of single passage results, respectively, and the stage total pressure ratio to within 1.4%. This confirms the model is a sufficiently accurate alternative to full wheel URANS simulations in conducting an inflow distortion study. Finally, the expected computational time of each section of the automated system as well as the overall time is discussed. The total computational cost associated with the automated model calibration is 23 core-days. Although this cost is relatively high, the system's capability of producing a model that performs similarly to a user-generated version bodes well, as this is the focus of the work. The alternative of running full-wheel URANS simulations is roughly 100 times more expensive than running a simulation of the calibrated body force model (depending on the number of inlet distortions being examined). The main advantage of the work

produced by this thesis is the removal of nearly all required user interaction during model calibration.

5.2 Conclusions

The objective of this thesis is to automate to the furthest extent the process of body force model calibration for a given compressor or fan geometry. As well, the typical process of fine-tuning viscous force model coefficients is instead subjected to a Nelder-Mead optimization procedure. These objectives are successfully achieved, and the accuracy of the model developed is on par with a user-generated version of the same model at the peak efficiency operating condition, as seen in Section 4.1. Unfortunately, the model's ability to match single passage reported stage isentropic efficiency is not as accurate as the agreement with regards to rotor isentropic efficiency. This could be attributed to the fact that the stage isentropic efficiency is not the ideal parameter to use when optimizing the viscous loss model coefficients associated with the stator blade row. In future work, making use of an alternative parameter to calibrate the model's losses associated with the stator blade row could reduce the minima found during the stator's viscous force coefficient optimization. The operating points chosen for the speedline during this study were relatively widely spread across the speedline. Subjecting the optimization procedure to operating points centred closer to the peak efficiency point could result in a decrease in the minima of the objective functions. The effect of not modelling blade metal blockage becomes significant when comparing results at operating points nearing choke conditions, as the model is unable to capture the drop-off in rotor work at these conditions. These discrepancies were not addressed during this study as time constraints did not allow for it; however, they can be addressed in future work.

5.3 Potential Future Improvements

While determining the compressibility correction is necessary in the normal force model calibration, it also has a detrimental effect on the model's ability to produce accurate chordwise blade loading. The latter is desirable in terms of aeromechanical forced response prediction, as accurate predictions of the spanwise and chordwise loading distributions are crucial aspects of the modal response of the blades. In the current modelling approach, the geometric parameters outlined in Section 3.4.2 are expressed as a function of span fraction. Mapping the geometric parameters as functions of both span and chord fraction could serve to reduce the effect of non-physical work removal found near the rotor's leading edge. Also, imposing constraints on the compressibility corrections to prevent work removal would serve as a method to improve this issue.

As previously mentioned, calibrating the stator blade row's parallel force model using the stage isentropic efficiency results in relatively large RMS error across the speedline chosen. A potential replacement for the calibration parameter is the stator's entropy loss coefficient, as it focuses on the entropy generation within the stator rather than the stage efficiency's combined effect of both blade rows. Although the minima found during the rotor's optimization procedure are much lower than the stator's, another possible parameter used for calibration of the rotor's loss model could be the loss coefficient.

Allowing the user to select the level of parallelization during model development is another potential improvement. Depending on the available computational resources, the wall-clock time associated with model calibration could be reduced by allowing the user to simultaneously produce speedline computations for both the single passage results used for calibration, as well as the body force model used during the optimization procedure.

The portion of the model calibration responsible for determining the compressibility correction required the most computational time during this study. This portion of the process could be accelerated by including an over-relaxation factor into Equation

3.8 responsible for determining the compressibility correction.

As mentioned in Section 1.1, the current system is designed to handle a single stage compressor. Generalizing the algorithm to allow for multiple blade rows, or 1.5-stage configurations would effectively widen the system's applicability.

Bibliography

[1] D. J. Hill. Compressor performance scaling in the presence of non-uniform flow. Master's thesis, University of Windsor, 2017.

[2] F. Marble. Three-dimensional flow in turbomachines. *High Speed Aerodynamics and Jet Propulsion*, 10:83–166, 1964.

[3] Y. Gong, C.S. Tan, K.A. Gordon, and E.M. Greitzer. A computational model for short wavelength stall inception and development in multi-stage compressors. In American Society of Mechanical Engineers, editor, *ASME 1998 International Gas Turbine and Aerospace Congress and Exhibition*, pages V001T01A114–V001T01A114, 1998.

[4] A. Peters. *Ulta-short Nacelles for Low Fan Pressure Ratio Propulsors.* PhD thesis, MIT, Department of Aeronautics and Astronautics, February 2014.

[5] D.K. Hall, E.M. Greitzer, and C.S. Tan. Analysis of fan stage design attributes for boundary layer ingestion. *J. Turbomach.*, 139:071012–1–071012–10, July 2017. American Society of Mechanical Engineers.

[6] V. Zwass. Expert system. Brittanica, 2017. Acessed on August 27th, 2017 at https://www.britannica.com/technology/expert-system.

[7] J. Seok, J. Kasa-Vubu, M. DiPietro, and A. Girard. Expert system for automated bone age determination. *Expert Syst. Appl.*, (50):75–88, 2016.

[8] A. Ikram and U. Qamar. A rule-based expert system for earthquake prediction. *J. Intell. Inf. Syst.*, 43(2):205–230, 2014.

[9] S. Koziel and L. Leifsson. Mutli-level cfd-based airfoil shape optimization with automated low-fidelity model selection. *Procedia Comput. Sci.*, 18:889–898, 2013.

[10] S. J. Wright. Optimization. Britannica, 2017. Accessed on August 27th, 2017 at https://www.britannica.com/topic/optimization.

[11] Gradient-free optimization. Online, April 2012. Accessed on August 27th, 2017 at http://adl.stanford.edu/aa222.

[12] J.A. Nelder and R. Mead. A simplex method for function minimization. *Comput. J.*, 7:308–313, 1965.

[13] T. Osgood and Y. Huang. Calibration of laser scanner and camera fusion system for intelligent vehicles using nelder-mead optimization. *Meas. Sci. Technol.*, 24(3), March 2013.

[14] S. Abedi and F. Farhadi. Integration of cfd and nelder-mead algorithm for optimization of mocvd process in an atmospheric pressure vertical rotating disk reactor. *Int. Commun. Heat Mass*, 43:138–145, 2013.

[15] MathWorks Inc., Natick, MA. *MathWorks MATLAB Documentation*, 2017a edition, 2017.

[16] ANSYS Inc., Canonsburg, PA. *CFX-Solver Manager User's Guide*, 17.2 edition, August 2016.

[17] Pointwise Inc., Fort Worth, TX. *Pointwise User's Manual*, v18.0r2 edition, 2016.

[18] A.J. Strazisar, J.R. Wood, M.D. Hathaway, and K.L. Suder. Laser anemometer measurements in a transonic axial-flow fan rotor. Technical report, NASA, 1989.

[19] V.J. Fidalgo, C.A. Hall, and Y. Colin. A study of fan-distortion interaction within the nasa rotor 67 transonic stage. *J. Turbomach.*, 134(5):051011, 2012.

[20] ANSYS Inc., Canonsburg, PA. *ANSYS TurboGrid User's Guide*, 17.2 edition, August 2016.

[21] Advanced Clustering Technologies, 3148 Roanoke Rd, Kansas City, MO. *MicroHPC Workstation*, 2017.

[22] E.J. Gunn and C.A. Hall. Aerodynamics of boundary layer ingesting fans. In *ASME Turbo Expo 2014: Turbine Technical Conference and Exposition*. American Society of Mechanical Engineers, 2014.

Appendix A

Permission to Include Copyrighted Material

University of Windsor

Matheson West <>

Re: EXT: Figure Request

Peters, Andreas (GE Aviation) <> Thu, Oct 12, 2017 at 3:15 AM
To: Matheson West <>

Hi Matheson,

Thanks for checking. Please go ahead and use figure 3-1 from my thesis.

Best,

Andreas

From: Matheson West [mailto:]
Sent: Mittwoch, 11. Oktober 2017 21:52
To: Peters, Andreas (GE Aviation) <>
Subject: Re: EXT: Figure Request

Hello Dr. Peters,

Thank you for granting me permission to use this figure.

Following my oral defense, my committee requested I include a figure depicting the body force model's effect of replacing the physical blade with a domain consistent with the blade row swept volume, and Figure 3-1 in your PhD Thesis does a fantastic job of doing this. I was wondering if you could grant me permission to include this figure in my thesis. Thank you!

Matheson West

On Fri, Sep 15, 2017 at 12:23 PM, Peters, Andreas (GE Aviation) <> wrote:

> Hi Matheson,
>
> No problem - go ahead.
>
> Andreas
>
> On 15. Sep 2017, at 17:56, Matheson West <<mailto:>> wrote:
>
> Hello Dr. Peters,
>
> My name is Matheson West, and I am a graduate student at the University of Windsor. My advisor is Dr. Jeff Defoe, and I am currently in the last stages of writing my Masters Thesis. I am emailing you to request your permission to use a Figure you presented in your PhD Thesis. The specific figure is Figure 3-2 from your thesis, and I am seeking to

University of Windsor

Matheson West <>

Figure for Thesis

hill11g <> Wed, Sep 27, 2017 at 10:58 AM
To: Matheson West <>

Mat,

Yeah man, feel free to use whatever you want.

Jarrod.

-------- Original message --------
From: Matheson West <>
Date: 2017-09-27 10:47 (GMT-05:00)
To: David Hill <>
Subject: Re: Figure for Thesis

Jarrod,

Thanks for all your help with everything I've done in my research thus far. I know I already asked if you would grant me permission to use Figure 3-17 from your thesis, but I was wondering if I could also use Figure 3-16 (with credit given to you of course!)? Thanks Jarrod.

Mat

On Fri, Sep 15, 2017 at 6:32 PM, <> wrote:

> Mat,
>
> The stator was from a source Dr. Defoe provided – which I think he got from his MIT colleagues.
>
> Jarrod.
>
> **From:** Matheson West [mailto:]
> **Sent:** Friday, September 15, 2017 12:01
> **To:** David Hill <>
> **Subject:** Re: Figure for Thesis
>
> Hey Jarrod,
>
> Sorry, another quick question for you. When you got the rotor blade data from the NASA technical report, did you have to find the stator blade data from a different source? Or was both sets of data from the NASA technical report? Thanks!
>
> Mat
>
> On Fri, Sep 15, 2017 at 10:07 AM, Matheson West <> wrote:

Vita Auctoris

Name: Matheson Gaelen West

Place of Birth: Walkerton, Ontario, Canada

Year of Birth: 1993

Education: M.A.Sc, Mechanical Engineering
University of Windsor, 2015-2017

B.A.Sc, Mechanical Engineering with Aerospace Option
University of Windsor, 2011-2015